	Final Technical Report:
Project Title:	**Hyperspectral Polymer Solar Cells, Integrated Power for Microsystems**
Covering Period:	July 1, 2008 to October 31, 2013
Date of Report:	May 27, 2014
Recipient:	Rochester Institute Technology
Award Number:	DE-FG36-08GO88110

Contacts:	Paul Stiebitz Phone: 585-475-2602 Fax: 585-475-5250 Email: phseie@rit.edu	Katherine Clark Phone: 585-475-7984 Fax: 585-475-7990 Email: kacsrs@rit.edu

DOE Project Team:	DOE Field Contracting Officer	-	Lalida Crawford
	DOE Field Project Officer	-	Andrew Kobusch
	Project Engineer	-	Leon Fabick

Introduction

Under this program, NanoPower Research Laboratories (NPRL) at Rochester Institute of Technology (RIT) has undertaken multifacetted research in energy conversion and storage. The research supports technologies that will find applications in autonomous microsystems, space energy systems, portable power systems, and terrestrial photovoltaic systems.

This report is organized into four sections:

- ***Integrated Power for Microsystems*** - The goal of this research is to increase the energy storage density of litium-ion batteries. The ability to achieve this relies heavily upon the ability to increase the cathode loading (capacity/cm^2), which in turn, allows for higher energy free-standing anodes to be properly paired.
- ***Strain Compensated Quantum Dot (QD) Photovoltaic Materials*** - This research focused on the use of both quantum dots (QD) and quantum wells (QW) for bandgap engineering of multi-junction solar cells composed of indium arsenide (InAs) QD and InGaAs QWs to spectrally "tune" the middle (GaAs) cell to a more favorable effective bandgap.
- ***Life Cycle Assessment of Organic Photovoltaics*** - The primary goal of this life cycle assessment is to compute the cumulative energy demand (CED) of various organic photovoltaic technologies, including single junction small molecule and polymer photovoltaics, as well as the multi-junction counterparts. A secondary goal is to examine the effect of specific processing conditions such as the use of thermal treatment, interface layers, low bandgap polymer and the type of heterojunction approach.
- ***Hyperspectral Polymer Photocells*** - The objective of this research is to produce a series of single junction polymeric solar cells using different NIR absorbing molecules and

combine them using nanocrystalline tunnel junctions to produce the polymeric analog to a multi-junction III-V solar cell.

This research represents the combined efforts of several RIT faculty and their students: Dr. Christopher Collison, Dr. David Forbes, Dr. Seth Hubbard, and Dr. Brian Landi.

Integrated Power for Microsystems

The purpose of this research is to address a critical technology barrier to the deployment of next generation autonomous microsystems – the availability of efficient and reliable power sources. The vast majority of research on microsystems has been directed toward the development and miniaturization of sensors and other devices that enhance their intelligence, physical, and networking capabilities. However, the research into power generating and power storage technologies has not keep pace with this development. This research leveraged the capabilities of RIT's NanoPower Research Laboratories (NPRL) in materials for advanced lithium ion batteries, nanostructured photovoltaics, and hybrid betavoltaics to develop reliable power sources for microsystems.

Advanced Lithium Ion Batteries

Carbon Nanotube Conductive Additives

The goal to increase energy density relies upon the ability to increase the thickness of the cathode composite. The necessity to increase the cathode loading (capacity/cm^2) will allow for higher energy free-standing anodes to be properly paired. Shown in ***Figure 1*** is an initial attempt to increase the cathode composite thickness dramatically over the state-of-the-art. It is shown that 125 um coatings are still mechanically stable, whereas, the 190 um coating delaminates. Attempts to enhance adhesion through the use of SWCNTs are essential to address this current limitation.

(a) 125 um coating after compression (b) 190 um coating after compression

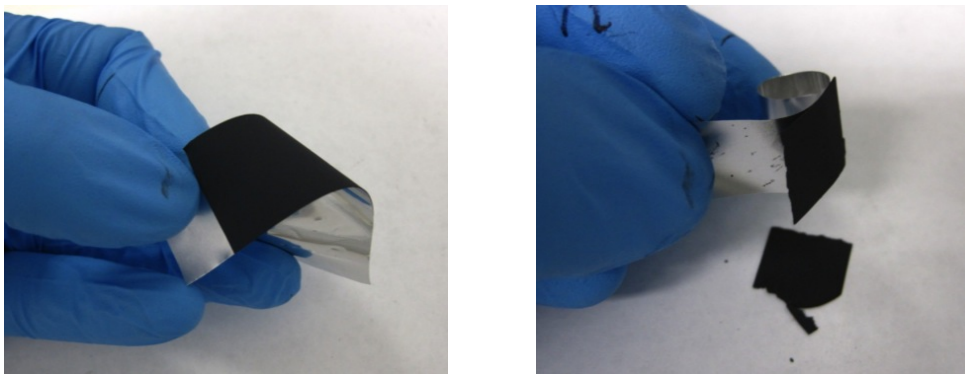

Figure 1: Images of cathode composites after compression for carbon black conductive additives for (a)125 um coating and (b)190 um coating.

An increase in areal capacity (mAh/cm^2) for battery electrodes results in an increase in the battery energy density (Wh/Kg). Strategies to increase the areal capacity include the use of higher capacity active materials and/or an increase in composite material thickness. In terms of the cathode, standard lithium nickel cobalt aluminum oxide (NCA) has a limit of ~200 um using traditional composite formulations with carbon black additives before de-lamination from the aluminum current collector. SWCNTs were incorporated into the NCA composite to enhance cathode thickness in the following ratio: 95%NCA:1%SWCNT:4%PVDF with 1% oxalic acid by weight. This addition allowed for an increase in total cathode thickness to ~ 300um before de-lamination onto a traditional aluminum foil current collector. In comparison, composite coating of an equivalent thickness onto an aluminum mesh resulted in better composite adhesion and the ability for consistent double sided coatings. Using the mesh, a maximum single sided thickness of ~800um was achieved before de-lamination was evident. Therefore, a tradeoff analysis is required to balance electrochemical performance (i.e. capacity and rate) with the increased thickness available using the developed designs.

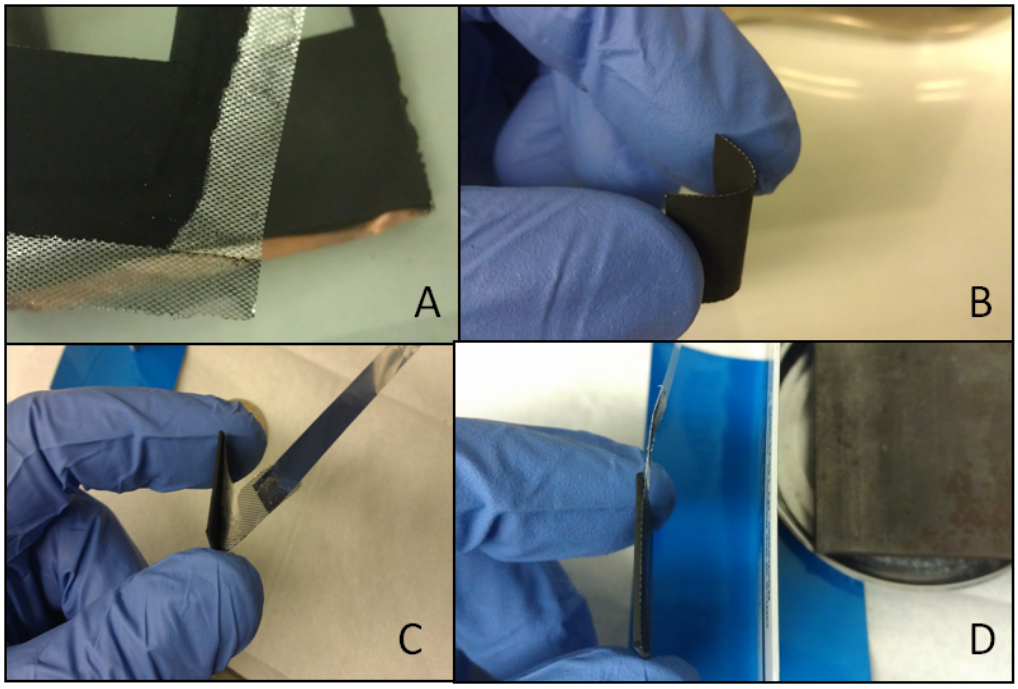

Figure 2 - Images of a cathode coating on top of (A) an Al mesh; (B) and resulting flexure stability. (C and D) The NCA composite is stable up to a thickness of approximately 800um.

Increasing the electrodes thickness with a constant length and width has the potential to increase the available power in a battery. The cathode composite of lithium nickel cobalt aluminum oxide (NCA) has a specific capacity of 180mAh/g. The thickness of an NCA composite was increased from 160um (3.7mAh/cm^2) to 320um (10.5mAh/cm^2) to increase the potential energy of the battery. This also increased the distance required for the lithium ions to travel which reduced the rate at which the battery could charge and discharge. Coin cells of 160um and 320um thick NCA cathodes were tested at C-rates of C/10, C/5 and C/2 vs. lithium. A trend was formed as the tradeoff of available energy and charge rate progressed. As the rate was increased from C/10 to C/2 for the 160um thick cathode the capacity was only reduced from 177mAh/g to 150mAh/g. A lower capacity was observed with the thicker (320um) cathode of 165mAh/g at C/10. This capacity diminished further to 117mAh/g at C/2.

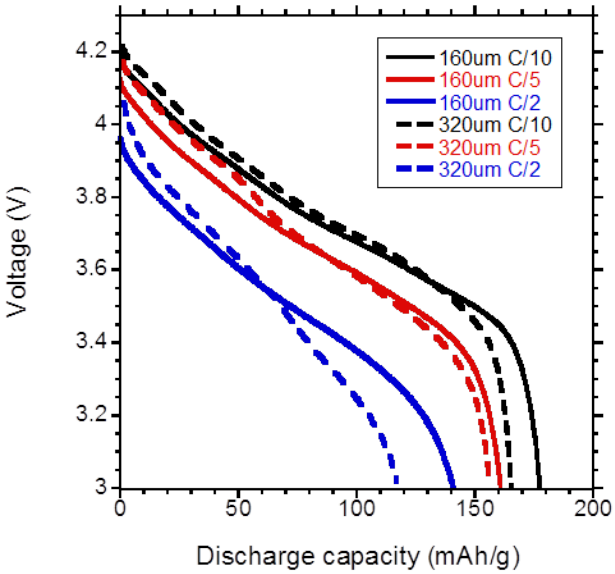

Figure 3: Discharge capacity comparison of coin cells with NCA vs lithium from 4.3v to 3v. Coin cells represented by the solid line had a cathode thickness of 160um. Coin cells represented by the dashed line had a cathode thickness of 320um. Each cell was discharged at C/10, C/5 and C/2.

The specific capacity of the cathode NCA is constant at 180mAh/g, whereas the total capacity of the full cell is dependent on the active mass of the cathode. An increase in the total mass of the active material directly results in an increase in capacity and energy of the full battery. This is accomplished by increasing the thickness of the cathode while keeping the length and width constant. As the thickness of the active material is increased the resistance increases, resulting in a potential for a loss in electrode capacity. A result of less than the specific capacity of the cathode illustrates a loss in battery performance. Traditional cathode materials use carbon black as a conductive additive. This additive performs adequately at thicknesses of typically less than 160um. Single walled carbon nanotubes (SWCNT) have shown a potential to stabilize the capacity at greater thicknesses and rates over that of carbon black. In this experiment, full cells were tested with a cathode thickness of 160um and 410um, increasing the active mass from 89mg to 267mg. The cathode composite with 4% carbon black additive were compared to those with only 1% SWCNT additive. The cells were tested at rates of C/10, C/5, C/2 and 1C. As the rate increased from C/10 to 1C all cells experienced a drop in capacity as expected. In the 160um thick sample case, using carbon black the specific capacity of the cell decreased from ~180mAh/g at C/10 to 102mAh/g at 1C. The same size sample using the SWCNT additive only decreased to 157 mAh/g at 1C. This is a 55mAh/g increase in performance over the standard composite. In the 410um thick sample using carbon black the specific capacity of the cell decreased from ~160mAh/g at C/10 to 56mAh/g at C/2 and only 5mAh/g at 1C. The same size sample using the SWCNT additive started at ~170mAh/g at C/10, marking an immediate improvement over the standard composite. The capacity decreased to 145 mAh/g at C/2 and 58

at 1C. This is a 89mAh/g increase at C/2 and a 53mAh/g improvement in performance at 1C over the standard composite.

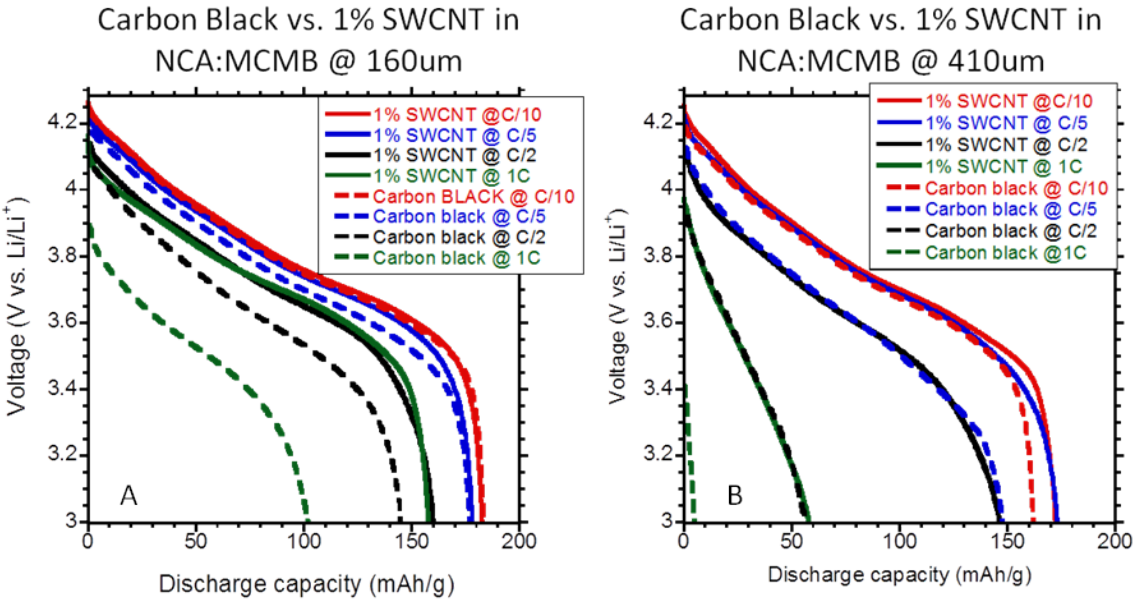

Figure 4: (a) Discharge capacities of 160um thick NCA cathode composite full cells using carbon black and SWCNT additives. Each cell was tested at C/10, C/5, C/2 and 1C. (b) Discharge capacities of 410um thick NCA cathode composite full cells using carbon black and SWCNT additives. Each cell was tested at C/10, C/5, C/2 and 1C.

High Voltage (LiMPO4) Cathode Materials

$LiCoPO_4$ cathode materials were tested in half cells opposite lithium. To understand the cyclability of the cathode, the half cells were allowed to run until a significant loss in capacity was observed. ***Figure 5*** shows how the $LiCoPO_4$ material cycled. The half cells were charged and discharged from 3V to 5V with a constant voltage step included. 1M $LiPF_6$ EC:EMC electrolyte was used. A linear loss in capacity was observed as the half cells cycled. It is believed that breakdown of the electrolyte is the primary cause of the capacity fade. It has been reported the carbonates are not stable above 4.6V making it difficult to maintain a stable capacity with time. Alternative electrolytes must be sought in order to take advantage of the high voltage potential presented by $LiCoPO_4$.

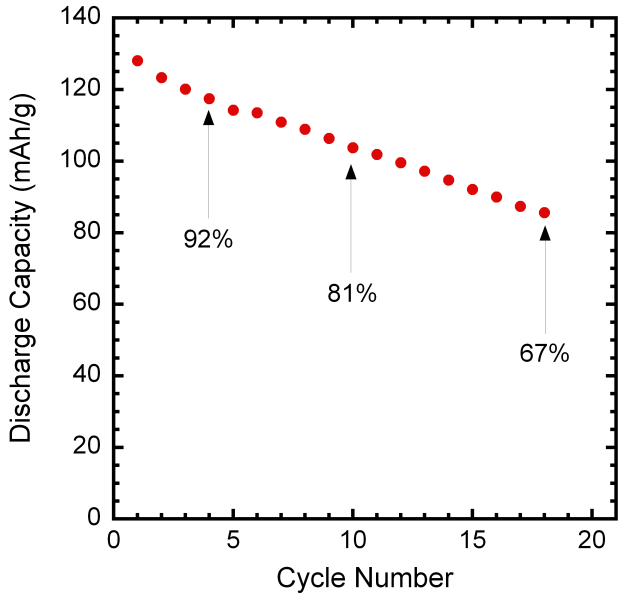

Figure 5: Discharge capacities of $LiCoPO_4$ as a function of cycle. Half cells were charged and discharged between 3V and 5V. Electrolyte used was 1M $LiPF_6$ EC:EMC.

Lithium metal phosphates have been investigated as alternative cathode materials for their potential to operate at higher voltage conditions. Most common cathodes have a voltage limit of ~4.5 volts. An increase in cathode voltage would result in an increase in battery energy density, however most electrolytes are unstable at higher voltages and breakdown causing the battery to fail. An evaluation of lithium bis(oxalato) borate (Li BOB) as an electrolyte stabilizer was performed on the as-synthesized $LiCoPO_4$ materials. The results show that an increased capacity of 135 mAh/g can be achieved vs. lithium in comparison to the control electrolyte.

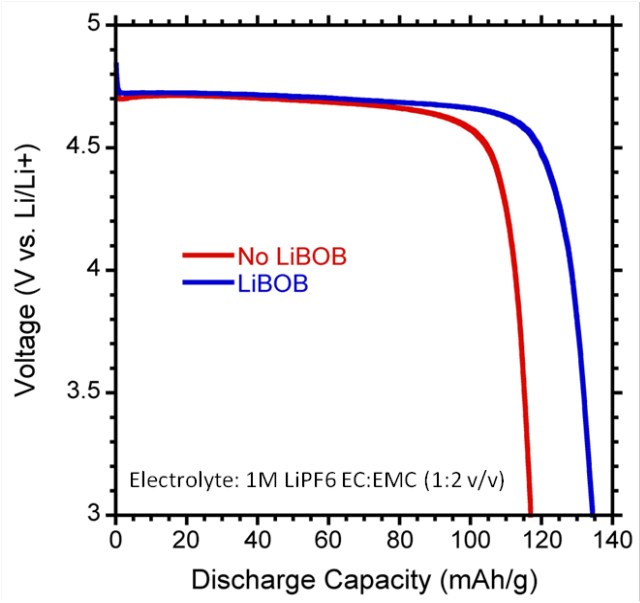

Figure 6 - Two lithium cobalt phosphate half cells are discharged from 4.8v to 3v. The half cell without the LiBOB has a capacity of only ~116mAh/g. The cell with the stabilizer is able to achieve an improvement to ~135mAh/g.

Figure ***7*** shows the discharge capacities for the base-to-acid ratios studied in this work. A series of base (NH_4OH) and acid (H_3PO_4) molar ratios were examined to determine an optimal condition for achieving the maximum capacity from the $LiCoPO_4$ active material. The highest intrinsic capacity observed is for a base-to-acid ratio of 0.2:1 with a maximum capacity of 128 mAh/g. This capacity is slightly higher than the average capacity of 120 mAh/g which has been reported by others. The decrease in capacity at the higher base-to-acid ratios can most likely be attributed to alterations in the pH of the solution. Previous reports for hydrothermal synthesis of $LiCoPO_4$ showed that the pH of the solution significantly impacted the size and morphology of the final product after reaction translating to a change in overall performance of the cathode active material.

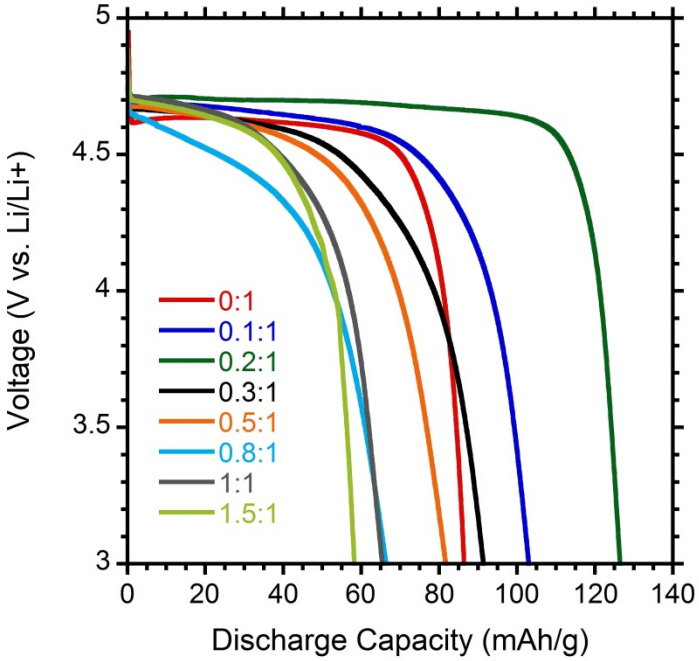

Figure 7: Discharge capacity comparison for $LiCoPO_4$ synthesized at NH_4OH:H_3PO_4 ratios between 0 and 1.5. Coin cells cycled between 3 V and 5 V with a constant voltage step at 5 V to 5% constant current.

Previous work with $LiFePO_4$ and $LiMnPO_4$ has shown that incorporation of a constant voltage (CV) step promotes an increase in discharge capacity due to the achievement of a fully delithiated state after charging. An analysis was done to understand the effects of including a constant voltage step during charging of the $LiCoPO_4$ cathode. Four CV conditions were considered: No CV step, CV @ 5 V vs. Li/Li^+ to 5% constant current (CC), CV to 25% CC, and CV to 50% CC. Coin cells were charged and discharged between 3 V and 5 V.

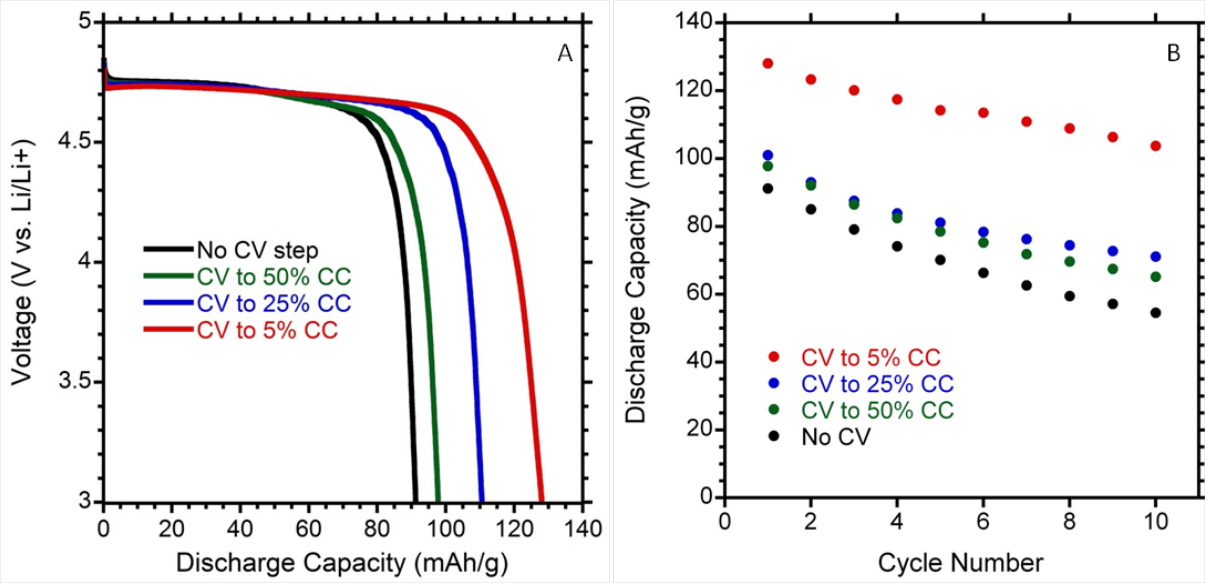

Figure 8 (a) shows the discharge profiles for each of the cases tested. Not including a CV step yields the lowest capacity of 91 mAh/g most likely due to an incomplete delithiation of $LiCoPO_4$. It is known that $LiCoPO_4$ undergoes a phase change to $CoPO_4$ as the cathode is charged . As the CV step is extended from 50% CC to 5% CC, thereby increasing the time at which the cells are in the charge phase, the discharge capacity improves significantly up to 128 mAh/g for a CV step to 5% CC. This indicates that a fully delithiated state is potentially reached therefore maximizing lithiation on discharge as suggested by previous studies. It is noted that the coulombic efficiency for all cases is approximately 60%.

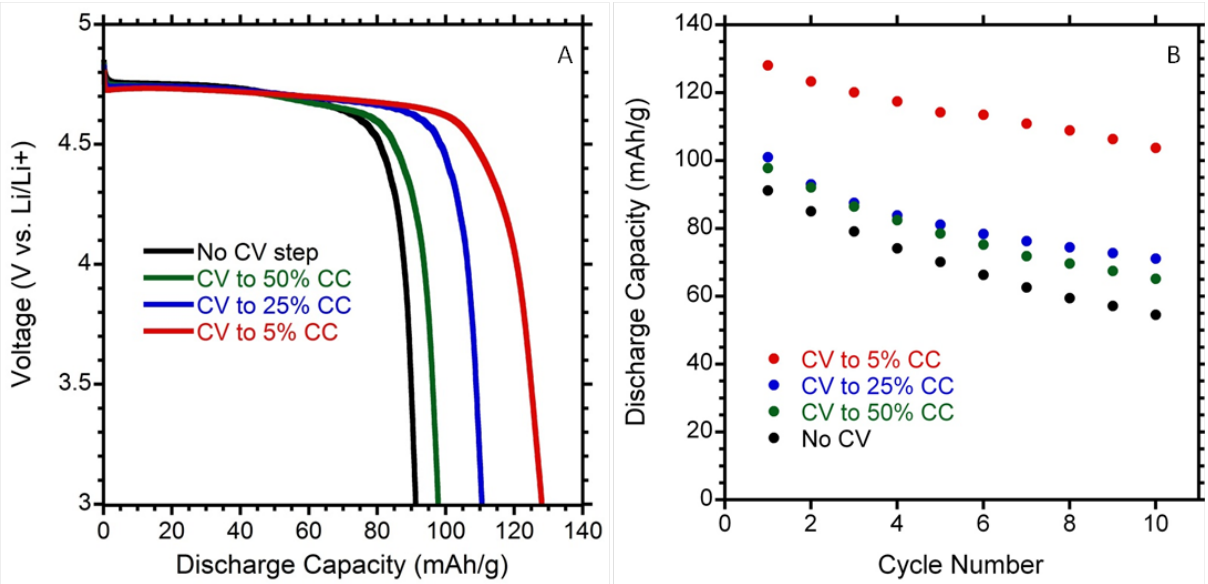

Figure 8 (b) shows the cycling behavior for each of the CV cases. In all four conditions, there is a decrease in the capacity over the course of 10 cycles with a 20% capacity fade for the best case of a CV to 5% CC. The 80% capacity retention after 10 cycles for the intrinsic material is significantly better versus recent reports combining $LiCoPO_4$ with a conductive source like

carbon nanotubes. It is known that the organic electrolyte will break down above a voltage of 4.6. Given that $LiCoPO_4$ requires a minimum voltage of 4.8 V for charge and discharge, the loss in capacity can most likely be associated with this phenomenon. Improvements in the electrolyte will be necessary in order to overcome this barrier and achieve a stable capacity necessary for applications of interest. However, progress with $LiCoPO_4$ continues towards development of a stable active material that can be used in advanced battery applications.

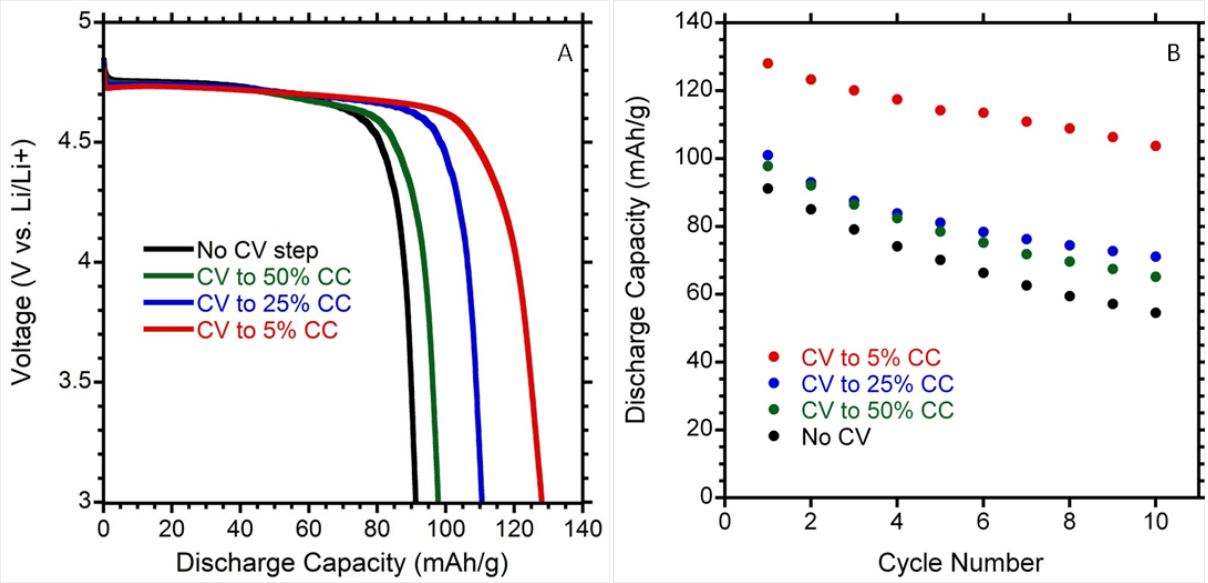

Figure 8: (a) Discharge capacities of $LiCoPO_4$ (0.2:1 base-to-acid) as a function of charging protocol. Half cells charged to 5 V and held with a) no constant voltage and under constant voltage (5 V) conditions to b) 50%, c) 25%, and d) 5% the initial constant current. Electrolyte used was 1M $LiPF_6$ 1:2 EC:EMC (v/v). (b) Cycling profile for each CV condition up to 10 cycles.

Free-standing Carbon Nanotube Anodes

Electrochemical testing to measure the lithium ion capacity as a function of weight ratio (Ge-NP:SWCNT:Ti) and rate capability has been performed for two hybrid ratios of 75:15:10 and 80:10:10 at constant currents of 50, 100, 200, 500, 1000, and 2000 mA g^{-1} using a 1 M $LiPF_6$ EC:PC:DEC electrolyte. The anode specific capacities (including the total electrode mass) are provided in ***Figure 9*** as a function of cycle number. The 75:15:10 hybrid shows nearly 200 mAh g^{-1} higher extraction capacity than the 80:10:10 electrode over the intial two cycles which were from 5 mV – 3 V, approaching 1000 mAh g^{-1} on the second cycle. The first two conditioning cycles spanned 5 mV – 3V in order to ensure the complete formation of the solid electrolyte interphase on the entire electrode. The subsequent 25 cycles are from 5 mV – 1 V to represent the major capacity contribution from the Ge-NPs, as the SWCNTs used in this work only exhibit ~110 mAh/g below 1 V based upon previous measurements and given the weight ratio used the maximum contribution to the hybrid capacity is ~10-20 mAh/g or 2-3%. The 75:15:10 hybrid shows consistently higher capacity and better cycling across the different rates suggesting the higher amount of SWCNTs are able to create an improved electrical percolation network and maintain pathways for lithiation. Although both hybrid electrodes show excellent stability at low

rate, the 75:15:10 maintains good performance at a 1C rate with an electrode capacity of 550 mAh g^{-1} at a 1 V cutoff voltage and a capacity greater than 300 mAh g^{-1} is still maintained at a 2C rate. The capacity of 550 mAh g^{-1} at a 1C rate (1 V cutoff voltage) for the hybrid free-standing electrode is more than double recent values for Ge thin-film CNT electrodes, illustrating the advantage of the 3-D electrode architecture.

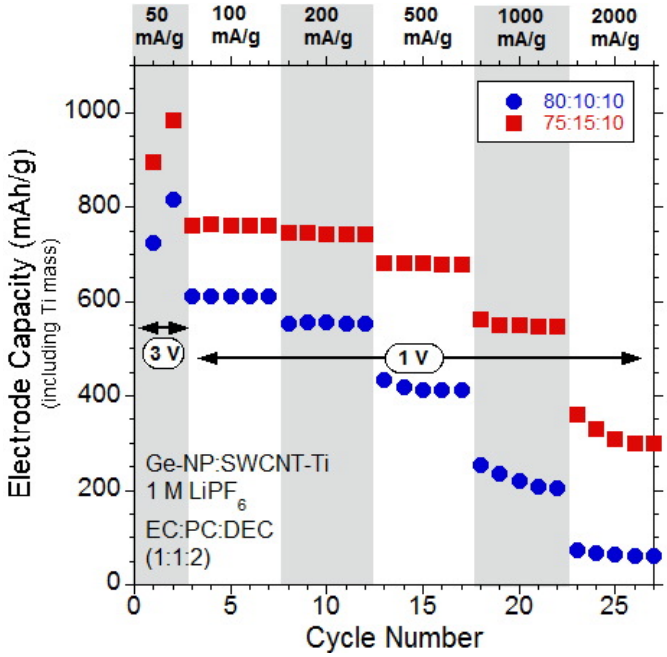

Figure 9: Electrode specific capacity of Ge-NP:SWCNT-Ti hybrid electrodes at two weight loadings, 75:15:10 (squares) and 80:10:10 (circles), at constant currents during insertion and extraction of 50, 100, 200, 500, 1000, and 2000 mA g-1. The first two cycles from 5 mV – 3 V and the subsequent cycles from 5 mV – 1 V.

Ge-NP:SWCNT hybrid anode materials exhibit high surface areas on the order of 1000 m^2/g. This provides an increased number of storage sites for lithium ions but also for excess formation of the solid-electrolyte-interphase (SEI). A larger SEI layer will result in a large first cycle irreversible capacity and low coulombic efficiency. Chemical vapor deposition (CVD) of silicon has the capability to reduce the surface area of SWCNT-based electrodes and fill void spaces, significantly improving the first cycle coulombic efficiency. The SWCNT bundle surface area is significantly reduced from 1000 m^2/g to 113 m^2/g, as measured using the BET method in a surface area analyzer. The silicon deposition improved the first cycle coulombic efficiency from ~74% to ~ 86%, as well as increasing the reversible capacity to >1200 mAh/g.

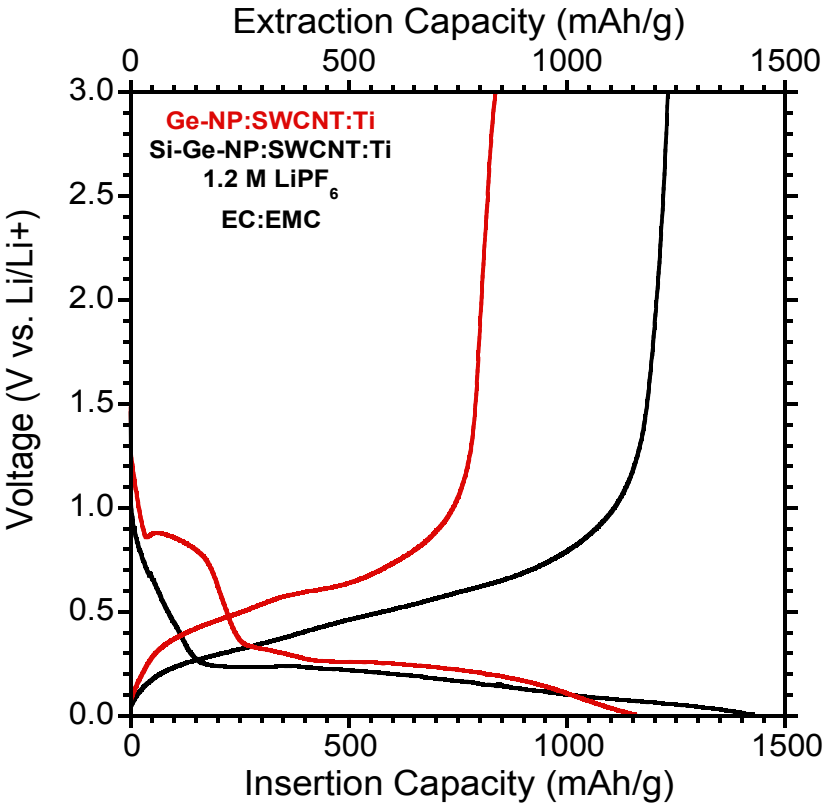

Figure 10 - The first cycle insertion and extraction capacities were evaluated with a columbic efficiency of ~74%. Si was then deposited onto the Ge-NP, reducing the surface area and SEI layer resulting in an increase in coulombic efficiency to 86%.

The energy storage of a battery can also be increased by increasing the number of electrode pairs within the pouch. This allows for an increase in active material while keeping the distance a lithium ion must travel to a minimum. The majority of the pouch cell mass is from the electrolyte and the laminate, therefore an additional set of electrodes will not double the total mass of the pouch thus yielding an increase in energy density (Wh/kg). Two pouch cells were fabricated using NCA (95%), PVDF (4%) and SWCNT (1%) as the cathode and MCMB (92%) PVDF (6%) and Super P (2%) as the anode. The discharge increased from 31.9mAh for the single electrode pair to 64.4mAh with the double electrode pair. As a result of the discharge capacity doubling without the total mass doubling the energy density was increased from 129Wh/kg to 180Wh/kg.

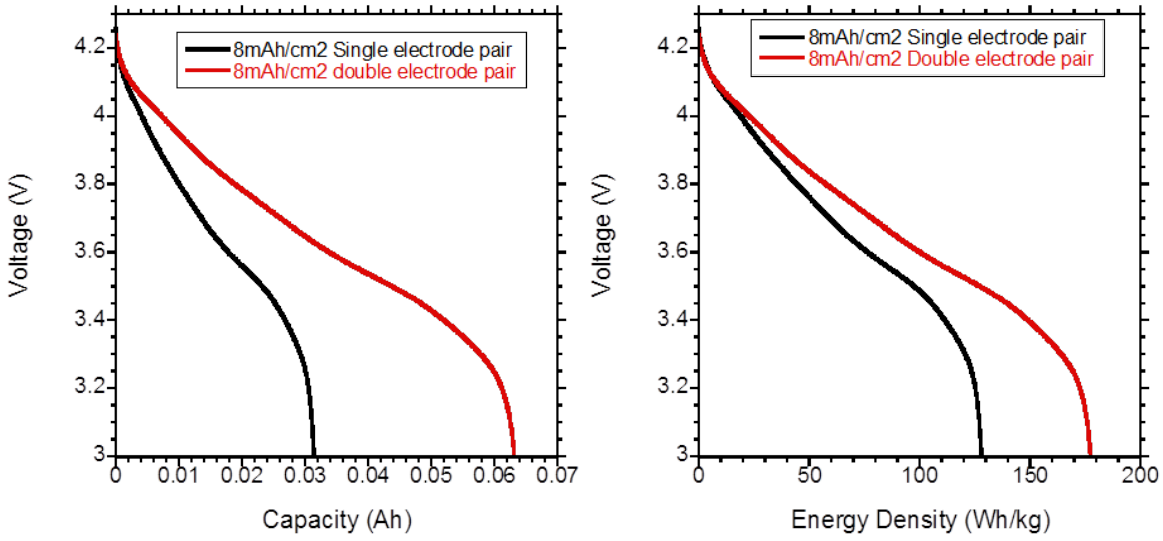

Figure 11: Left; Discharge capacity comparison for NCA(1% SWCNT):MCMB from 4.3v to 3v for the single and double electrode pairs. Right; Energy density of the single and double electrode pairs as each cell is discharged over the same voltage range. Each cell was discharged at a rate of C/10.

The energy density of a battery is represented by Wh/kg. This multiplies the total capacity of the battery by its average voltage and then divides by the total mass of the pouch cell. Several factors can be adjusted to increase the total energy density of a full cell such as increasing the active material, using materials with greater average voltages, reducing the excess mass of the full cell. Using multiple electrode pairs is one technique that incorporates multiple advantages. As demonstrated in sub task 1.1 a thickness limit is eventually reached beyond which the full cell suffers a loss in capacity. The use of multiple pairs allows the pouch cell to achieve the same total active mass as that of a much thicker single electrode cell, but still provide a shorter distance for the lithium ion to travel. The use of multiple pairs gives the opportunity to coat both sides of the current collector with the active material. This eliminates the mass that would have been added with additional current collectors. As each electrode pair is doubled, the total capacity of the battery is doubled. This doubles the watt hours of the battery. The total mass will not be doubled as the cathode and anode only make up a portion of the full cell. The majority of the total mass of the full cell is from the laminate packaging and electrolyte. This trend cannot continue indefinitely however, eventually there is a point of diminishing returns where the percent increase in capacity matches the percent increase in total mass. Full cells using the standard NCA:MCMB composites with an increase in the thickness of the active cathode mass of 160um, 280um and 410um have been calculated out to these end points. A substantial increase in energy density is observed when increasing from one electron pair per cell to two. The energy density is increased further at four electrode pairs. This is approximately an additional 25% increase over the two pair improvement. Beyond 4 pairs additional electrode pairs contribute to a negligible increase in energy density. After 10 electrode pairs any additional pair would increase

the energy density by less than 0.5Wh/kg. An energy density of 250Wh/kg is achievable in full cells with a cathode composite thickness of 410um.

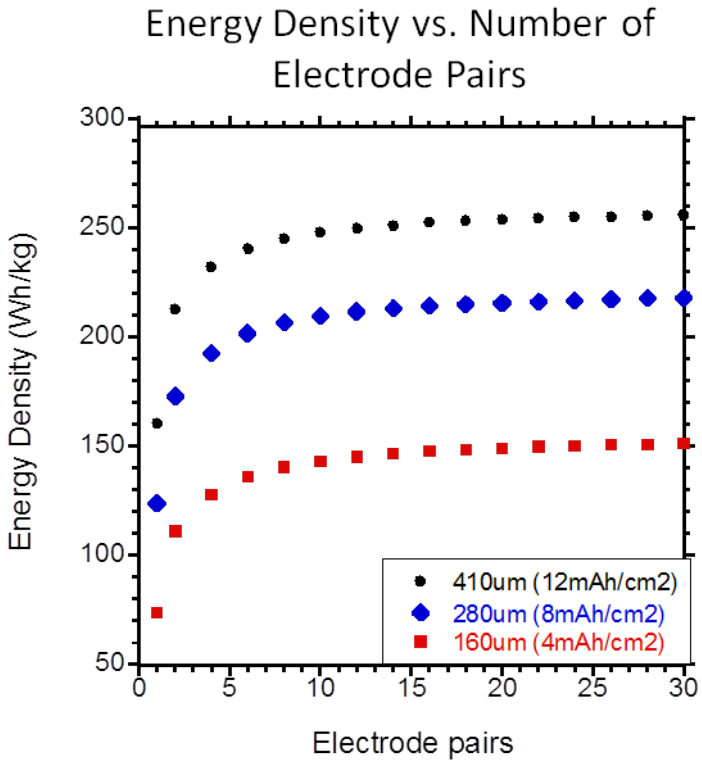

Figure 12: The energy density for traditional NCA:MCMB multi pair pouch cells was calculated with cathode composite thicknesses of 160um, 280um and 410um. A brief increase is observed with the initial increase in electrode pairs followed by diminishing returns.

Novel Electrodes

The energy density of a battery is typically measured in Wh/Kg. There are several approaches to increasing the energy density of a battery. Adding additional anode/cathode pairs will increase the capacity resulting in an increase in watt-hours. It will also lead to an increase in mass; however, the anode/cathode pair only entails a fraction of the total mass resulting in a net increase in energy density. There is a limit to this expected increase as the percent increase in capacity will eventually equal the percent increase in total battery mass. The expected values for multiple layers of anode/ cathode pairs were calculated and are presented in *Figure 12***.** An increase in energy density is realized as the number of pairs increases; however, no significant gain in energy is attained beyond 4 pairs. Anode and cathode slurries were created from commercially available mesoporous carbon microbeads (MCMB) and lithium nickel cobalt aluminum oxide (NCA). Multiple layer pouches were measured and compared to expected results as shown in the ***Figure 13.*** The measured results followed theoretically predicted values.

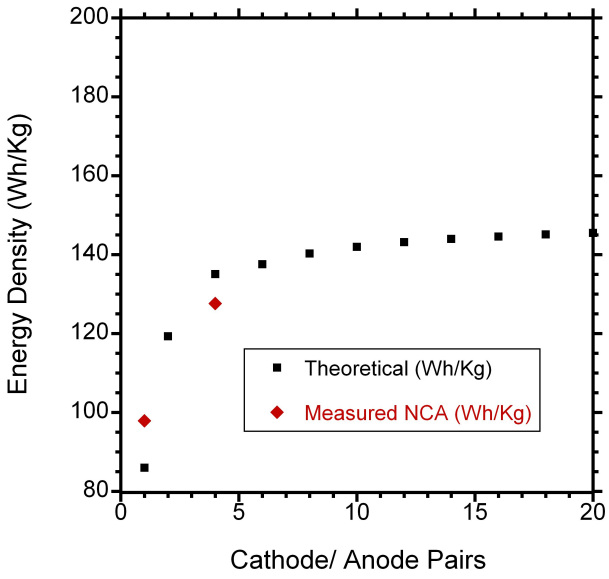

Figure 13: Energy density as a function of cathode-anode pairs in RIT designed pouch cell.

Since the energy density of a full pouch cell battery is measured by Wh/kg another method to immediately increase the energy density is through reduction of the total mass of the pouch. The mass of the pouch is comprised of the active material, metal substrates, electrolyte, separator and laminate. The minimum volume of electrolyte needed to maintain a functional pouch cell was investigated. A standard NCA:MCMB pouch cell was constructed with an electrode areal capacity of 8mAh/cm^2. The total mass for each pouch cell prior to the addition of electrolyte was 613 mg. Electrolyte was filled to the first pouch until complete saturation was visible, adding 444 mg. The electrolyte mass was reduced in the second pouch cell to half that of the original. The surfaces of all the active materials and the separator were saturated, leaving no excess electrolyte in the pouch. By reducing the total mass of the pouch through electrolyte optimization the energy density was increased from 110Wh/kg to 128Wh/kg.

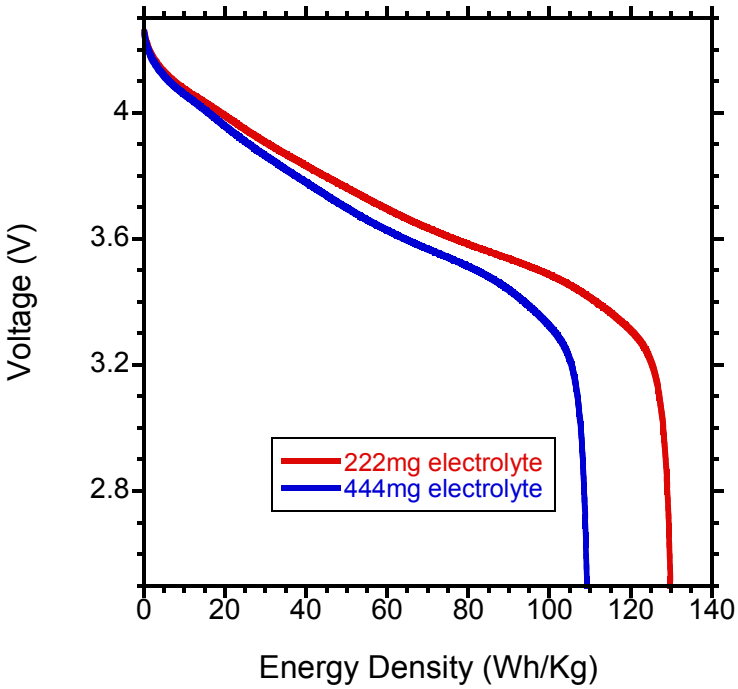

Figure 14 - The energy density of two NCA:MCMB 8mAh/cm^2 pouch cells were compared. The first pouch cell used 444mg of electrolyte, about 41% of the total mass. The second pouch cell used a reduced electrolyte mass of 222mg, about 25% of the total mass. Both pouch cells reached the same capacity but the cell with a reduced mass had a 19% increase in energy density.

Prior electrochemical performance on Ge-NP:SWCNT electrodes demonstrated stable cycling at modest cycling rates. The rate capability of the hetero-hybrid containing both silicon and germanium was compared with a Ge-NP:SWCNT electrode versus lithium at currents of 50 to 1000 mA g^{-1}. *Figure **15*** shows the first two conditioning cycle capacities at a 3 V vs. Li/Li$^+$ cut-off voltage with the remaining cycles having a cut-off voltage of 1.5 V vs. Li/Li$^+$ to focus on the lithium storage in Si and Ge active materials; and the insertion current was held constant at 100 mA g^{-1} after the first two cycles. The hetero-hybrid electrode has a capacity over 1200 mAh g^{-1} at low cycling rates as compared to the Ge-NP:SWCNT:Ti hybrid with a capacity just over 800 mAh g^{-1}; additionally the hybrids have increases in extraction capacity over the first 2 cycles as seen with other electrodes containing germanium. As the extraction current is increased to 1000 mA g^{-1} the hetero-hybrid electrode extraction capacities are reduced to 500 mAh g^{-1}. The larger reduction in capacity of the hetero-hybird as compared to the Ge-NP:SWCNT electrode as extraction current is increased beyond 200 mA g^{-1} is suggestive of the reduced storage contribution of the silicon at the higher extraction rates. This also highlights the need to balance the constituent materials in order to optimize the electrochemical performance based upon storage capacity, rate capability, and coulombic efficiency.

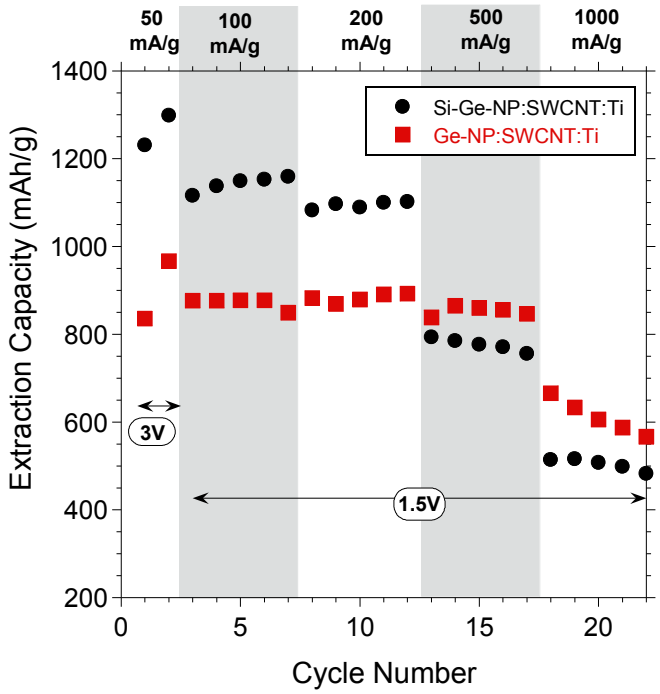

Figure 15: Extraction capacities of Ge-NP:SWCNT hybrids and Si-Ge-NP:SWCNT hybrids as extraction current is increased from 50 mA g^{-1} to 1000 mA g^{-1}. The first two conditioning cycles had a cut-off voltage of 3 V vs. Li/Li^+ and the following cycles had a cut-off voltage of 1.5 V vs. Li/Li^+.

A lower surface area leading to a reduction in SEI formation was found to improve the safety of Ge-NP:SWCNT hybrid electrodes as measured by differential scanning calorimetry (DSC) which can be seen in *Figure 16***.** DSC can be used to measure the exothermic energy released from an electrode, the temperature at which it occurs, and the intensity of the reaction, which all have implication in the contribution the materials could have towards thermal runaway. Thermal runaway in lithium ion batteries typically begins in a fully charged cell on the anode where the breakdown of the solid-electrolyte-interface (SEI), around 150°C, releases heat and increases the cell temperature. The active anode material and polymer binder will then react at higher temperatures. The DSC curves were normalized to capacity to compare anodes of varying capacities. The pure SWCNT paper has a significant SEI formation due to the high surface area SWCNTs which results in a lower reaction initiation temperature of 125°C and a greater reaction intensity of 7.06 J mAh^{-1}, as compared to conventional MCMB composites with a value of 5.14 J mAh^{-1}. Therefore, a pure SWCNT paper would initiate a thermal runaway reaction at a lower temperature. When SWCNTs and Ge-NPs are mixed, the exothermic energy released is reduced to 4.26 J mAh^{-1} compared to 7.06 J mAh^{-1} for the pure SWCNT sample. When Si is coated on the Ge-NP:SWCNT electrode, there is a higher capacity, and the reduced SEI formation results in a shift in the starting reaction temperature to 160°C and a significant reduction in peak intensity and exothermic energy released (2.77 J mAh^{-1}). It is no longer sufficient to only consider increased storage capacity of nanomaterial anodes, and the importance of safety for novel nanostructured anodes is becoming more prominent. This silicon deposition approach to

free-standing anodes shows progress in tailoring nanomaterial anodes for higher capacities in conjunction with improved safety.

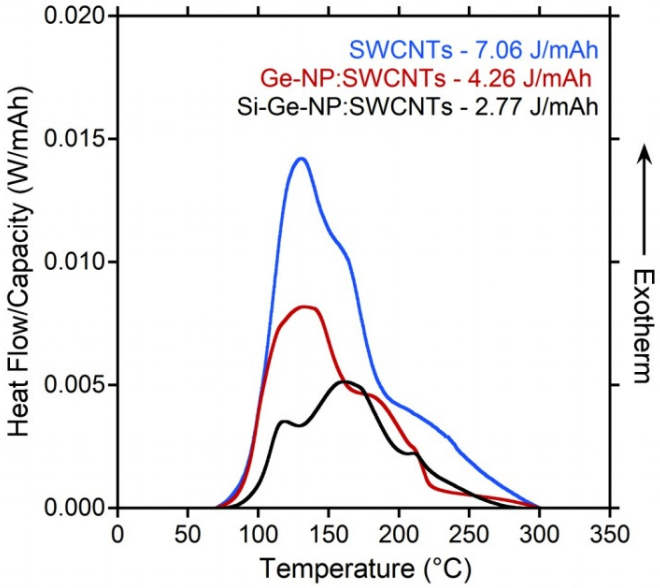

Figure 16: Differential Scanning Calorimetery (DSC) for SWCNT, Ge-NP:SWCNT, Si-Ge-NP-SWCNT anodes after one complete cycle and lithiation to a cell potential of 5 mV vs. Li/Li

Pathways to Enhance Battery Lifetimes

Coin cells were made for Ge-NP:SWCNT hybrids versus lithium with the standard electrolyte and stabilized for 1 hour before the first 'pre-cycle' measurement was taken (see ***Figure 17)***. Subsequent measurements were acquired after the corresponding cycle had reached complete lithium extraction at 3V vs. Li/Li+. The results suggest that the charge transfer component, corresponding to the width of the semicircle is decreasing over the initial cycles. Thus, the Ge-NP:SWCNT hybrids may be establishing a stable SEI for cycling during the conditioning cycles and future measurement in full batteries (paired against a cathode) will better assess the lifetime stability.

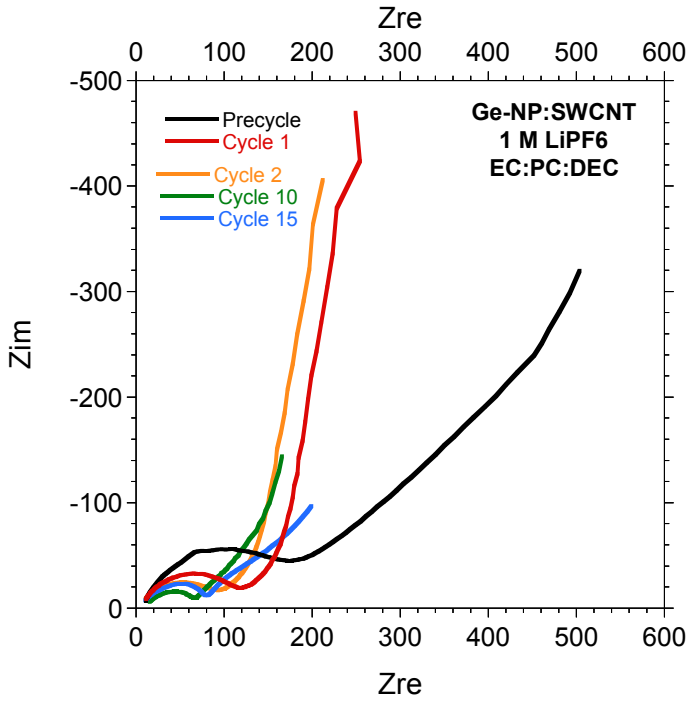

Figure 17: Electrochemical impedance data for a Ge-NP:SWCNT hybrid vs. lithium as a function of cycling.

Higher capacity Si-CNT anodes are an alternative to traditional MCMB anodes as a strategy to increase the capacity of lithium ion batteries. The capacity of these novel anodes is expected to increase with higher weight loadings of the silicon. Samples were created with an electrode areal capacity ranging from 3.5mAh/cm^2 to 11.5mAh/cm^2. At the high loadings, premature battery failure occurred and post mortem analysis reveals that the silicon films were ruptured. At lower weight loadings, the Si-CNT anodes were more stable and ongoing studies will examine ways to mitigate the failure at higher loading.

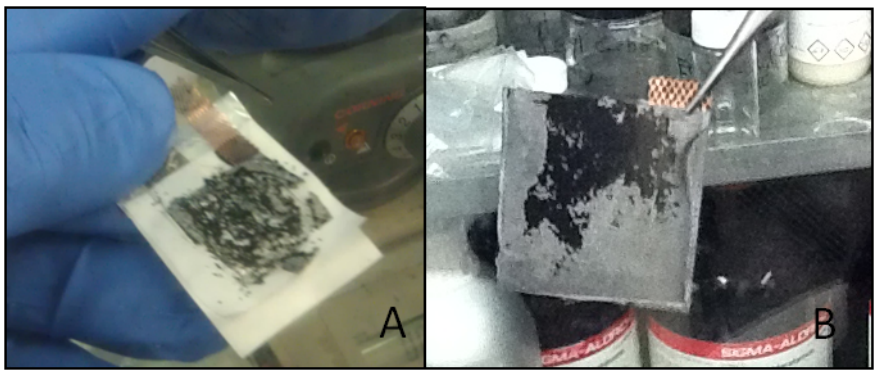

Figure 18 - An anode composite of Si-CNT deposited at 11.5mAh/cm^2 separated into individual pieces upon cycling (A). A lower weight loading of 3.5mAh/cm^2 has lost some Si coating but remains intact (B). The lower weight loading cell was still capable of cycling.

During the initial cycle of a lithium ion battery a portion of the electrolyte decomposes to create a SEI layer. This passivation layer is essential for optimal electrode performance. A significant amount of gas is evolved as a byproduct of the electrolyte decomposition. In a sealed environment such as a pouch cell this evolved gas will result in an increase in pressure hindering the batteries capacity or destroying it completely. The amount of gas generated is dependent on the type of electrolyte and anode composition. Cyclic voltammetry is an effective way to identify the evolution of the gas but may not reveal the exact volume released for each specific pouch cell. A bubbler system was designed to monitor the formation of gas throughout each pouch cells initial cycle. Santoprene rubber was heat sealed inside the standard pouch cell laminate to serve as a septum. A needle was inserted through the septum allowing each pouch cell to be inflated and inspected for leaks. The cells can now be placed under vacuum and submerged in mineral oil to observe the volume of gas escaping through the needle.

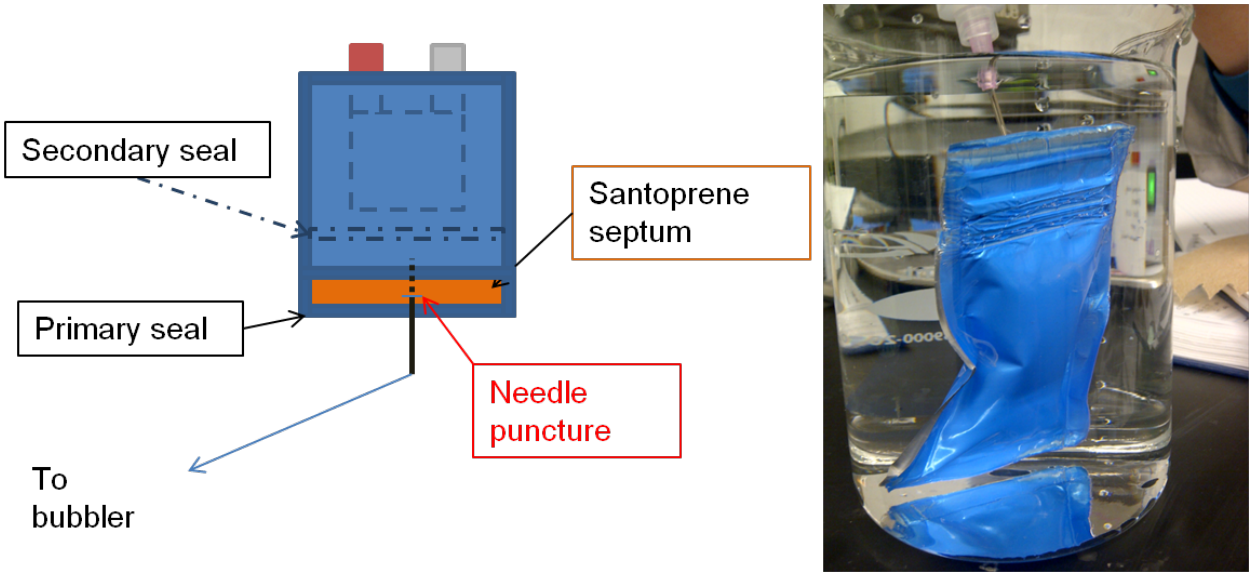

Figure 19: Left; A schematic diagram of the bubbler setup. Santoprene has a similar melting point as the laminate creating an air tight seal. Right; the pouch cell has been inflated and passed all leak tests. Next a vacuum will be drawn and the cell may be charged.

It is well known that during the first cycle of a lithium ion battery a SEI layer is formed as a portion of the electrolyte breaks down on the surface of the anode. A byproduct of this chemical breakdown results in the evolution of gas. With a properly sealed pouch cell there is no route for this gas to discharge, resulting in an increase in pressure exerted on the cell. Typically in a standard NCA:MCMB pouch cell, prior to cycling, a 15 psi force is applied. This force ensures adequate contact of the anode and cathode throughout the duration of its lifetime. A force greater than the initial 15 psi can be detrimental to the pouch cell performance, shortening the lifetime and causing failure. The volume of gas generated is related to volume of active material in the pouch cell. Pouch cells were constructed using NCA:MCMB with an areal capacity of 12mAh/cm^2. The volume of gas evolved was measured at approximately 12cm^3 for each cell as the pouch cells were cycled once. This volume of gas causes the pouch cell to swell much larger

than its starting volume adding a significant amount of pressure to the cell. As no gas is generated in subsequent cycles a secondary pouch should be constructed for better gas management. This secondary pouch would be removed after completion of the first cycle. The primary pouch will then be sealed leaving the pouch cell gas free to operate at its optimized pressure.

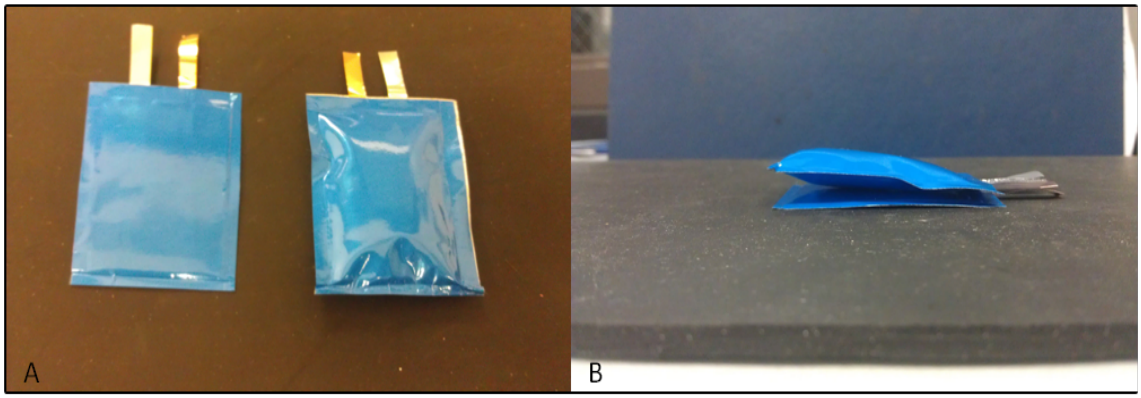

Figure 20: The volume of gas evolved during the first cycle was measures for 12mAh/cm^2 NCA:MCMB pouch cells. A) Left; prior to cycling, Right; after first cycle completion. B) Bottom; prior to cycling, Top; first cycle completion.

Strain Compensated Quantum Dot (QD) Photovoltaic Materials

This portion of the project focused on the use of both quantum dots (QD) and quantum wells (QW) for bandgap engineering of multi-junction solar cells. This work was focused both on a potential near term application, namely the use of indium arsenide (InAs) QD and InGaAs QWs to spectrally "tune" the middle (GaAs) cell of a state-of-the-art triple junction device to a more favorable effective bandgap, as well as the long term goal of demonstrating intermediate band solar cell effects. The QDs are confined within a high electric field i-region of a standard GaAs solar cell. The extended absorption spectrum (and thus enhanced short circuit current) of the QD solar cell results from the increase in the sub GaAs bandgap spectral response that is achievable as quantum dot layers are introduced into the i-region. We have previously grown InAs quantum dots by OMVPE technique and optimized the QD growth conditions. Arrays of up to 40 layers of strain balanced quantum dots have been experimentally demonstrated with good material quality, low residual stain and high PL intensity. Quantum dot enhanced solar cells were grown and tested under simulated one sun AM1.5 conditions. Concentrator solar cells have been grown and fabricated with 5-40 layers of QDs. Testing of these devices show the QD cells have improved efficiency under concentration compared to baseline devices without QDs. Improvements in a triple junction solar cell with the insertion of QDs into the middle current limiting junction was estimated to be as high as 36% under one sun illumination for a 100 layer stack QD enhanced cell. Listed below are the significant achievements over the course of this project.

Summary of Accomplishments

1. Growth optimization of InAs QDs on 2" GaAs wafers has resulted in improved uniformity of QD with very low QD coalescence. Standard deviation across a 2" GaAs wafer was reduced by over one order of magnitude using optimized growth conditions.
2. Demonstrated an open circuit voltage greater than 1.0V with corresponding current enhancement in a QD solar cell. This voltage is the highest reported open circuit voltage for a quantum dot solar cell.
3. Demonstrate that higher substrate misorientation causes a shift in QD critical thickness for nucleation as well as providing increased QD density and uniformity. This result is a useful guide for both academia and industry, since solar cells are often grown on highly misoriented substrates.
4. A quantum well solar cell design was developed, grown and tested. Successfully grew and fabricated InGaAs/GaAsP QW solar cells. All cells show sub-bandgap photo-conversion. Under one sun AM1.5 illumination the 10 layer MQW cells show improved short circuit current density (0.5 mA/cm^2).
5. A robust model for the QD and QW solar cell was developed in the physics-based software Crosslight APSYS. This model accurately accounts for QD current enhancement. Model used to predict performance for QD triple junction devices. Model is also being used to study new QD device designs.
6. We developed a modeling routine to simulate the performance of baseline and QD-enhanced *pin*-GaAs solar cells using the physics-based software Crosslight APSYS. Simulations suggest placing the QDs in regions of reduced recombination enables a recovery of open-circuit voltage (V_{OC}). Devices with the QDs placed in the center and near the doped regions of a pin-GaAs solar cell were experimentally investigated. While the V_{OC} of the emitter-shifted device was degraded, the center and base-shifted devices exhibited V_{OC} comparable to the baseline structure. A strong sensitivity to location largely dictated by local SRH recombination rates was observed.
7. The effects of incorporating a thin delta doping layer near the QDs to achieve this was studied both through computational modeling and device experimentation. Experimental 1-Sun AM0 results showed a monotonic voltage recovery with increasing electron doping levels, as well as a decrease in current density. The introduction of dopant reduced SRH recombination in the QDs, allowing for larger V_{OC} as compared to undoped cells. Due to the high thermal escape rate, additional experimentation at low temperature or high light concentration is necessary to explore conditions where evidence of a two-photon carrier extraction mechanism, as required for IBSC, can be shown.

Growth and Characterization of QD Based Solar Cells using a Thicker LT Cap

*Figure **21*** shows the EQE plot beyond 800 nm a the 10-period QD-enhanced GaAs p-i-n cells for each value of GaAs capping thickness. A baseline GaAs p-i-n cell is also included as a reference and clearly shows the increased below-GaAs-bandgap response due to the InAs QD. The EQE also increases as the capping thickness increases from 1.0 to 4.0 nm. Integrating the EQE data beyond 880 nm over the AM0 spectrum illustrates the increased Isc due to the QD structures and this trend is plotted in *Figure **22***. *Figure **22*** shows an increased Jsc as a function of the GaAs

capping thickness. In other words, capping the QD with 4.0 nm GaAs rather than 1.0 nm leads to an increased Isc response from 0.15 to 0.21 mA/cm^2 or a 40% increase simply by capping the QD with a slightly thicker layer. ***Figure 22*** also shows the effect of the LT-GaAs thickness on Voc. As the cap thickness increases, the Voc decreases from 980 mV (1.0 nm cap) to 925 mV (4.0 nm cap). The Voc data was obtained using average values for at least 8 cells across a 2" diameter wafer. The capping layer thickness over QD has a direct impact on the size of the QD. This change in QD size directly affects the transition energy of the buried QD which has an effect on the operating characteristics of QD-enhanced solar cells. We have demonstrated an increase in Jsc and corresponding decrease in Voc as a function of the capping thickness in QD-enhanced solar cells. These results are understandable when considering possible modification of the QD size due to the capping layer.

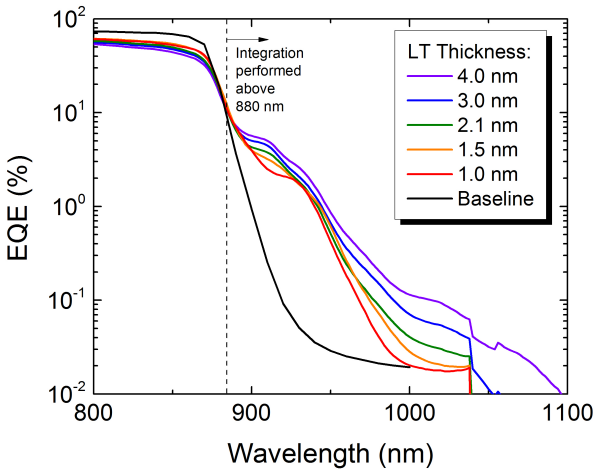

Figure 21: > 880 nm EQE illustrating the increased IR response due to increased GaAs capping thickness.

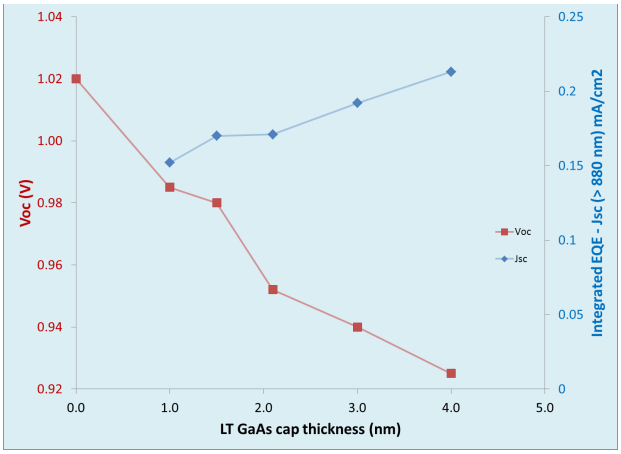

Figure 22: Increased Jsc between 880-1100 nm due to QD increases as a function of GaAs cap thickness.

Growth of New QD cell with High Level of δ-doping and Modeling of the δ-doping Effects

Simulation of device structure was performed using APSYS, a finite element analysis software package developed by Crosslight. Results showed decreased Shockley-Read-Hall recombination rates in QD devices incorporating doping, which indeed lead to increased voltage both in simulation and experimentally through the reduction of dark current and decrease in diode ideality factor. At the highest levels of doping, a reduction in bulk carrier collection was observed in the simulation and device results, as minority carriers experienced a reduced lifetime in the highly doped QD region.

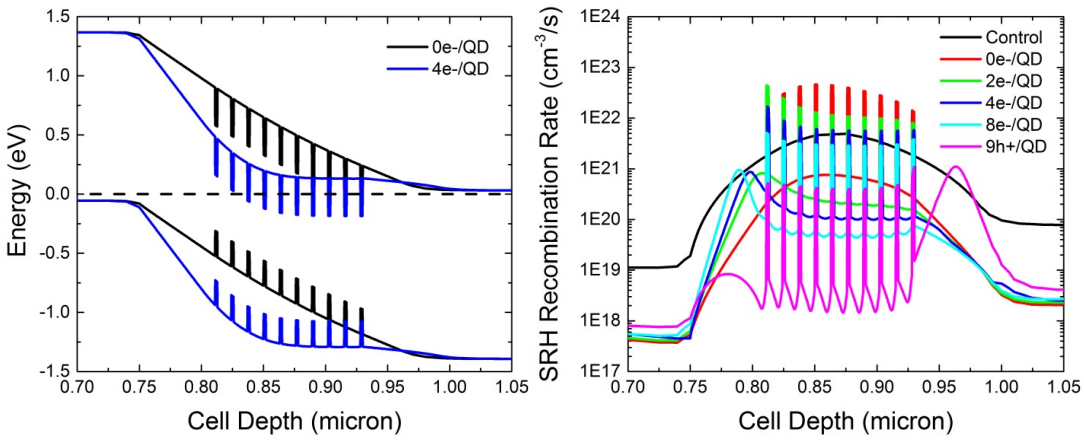

Figure 23: Simulated band structure of doped QD compared to undoped, as well as simulated Shockley-Read-Hall recombination in the quantum dot region.

Table 1: Experimentally determined figures of merit of various doping levels compared to control.

Sample	Jsc (mA/cm2)	Voc (mV)	FF (%)	Eff (%)	Dark Current (A/cm^2)	Ideality Factor	Integrated Jsc (350 nm – 1100 nm) (mA/cm^2)	Integrated Jsc (880 nm – 1100 nm) (mA/cm^2)
Control	22.15	1040	80.99	13.66	$1.13x10^{-18}$	1.08	22.97	0.079
0e-/QD	22.82	837	75.05	10.49	$1.89x10^{-10}$	1.77	23.62	0.291
2e-/QD	22.48	905	78.81	11.74	$9.19x10^{-13}$	1.45	23.76	0.298
4e-/QD	22.43	919	78.89	11.9	$2.86x10^{-15}$	1.2	23.45	0.289
8e-/QD	21.9	958	81.88	12.58	$3.35x10^{-17}$	1.09	22.91	0.265
9h+/QD	11.5	859	69.45	5.02	$3.19x10^{-10}$	1.9	10.33	0.136

An in-house 8-band k.p code for calculating optical properties of three-dimensional semiconductor nanostructures such as quantum dots was modified to also produce absorption

coefficient spectra for quantum wells. In order to account for excitonic effects, the ground state exciton contribution is approximated using a self-consistent Hartree approach where the wavefunctions of the ground electron and hole states in the QW are iteratively calculated in turns using the Coulombic potential from the other particle until convergence. This yields a more accurate estimate of the ground state absorption. Other excitons do not make a big enough contribution to the experimental spectra at room temperature due to the rapid decay of higher exciton states compared to the ground exciton, and are therefore not calculated. The resulting spectra is then added to the bulk GaAs spectrum, yielding a more accurate mix of simulated and experimental data for the simulation of solar cells. The absorption coefficient of a 10 nm In0.25Ga0.75As QW is shown in ***Figure 24***.

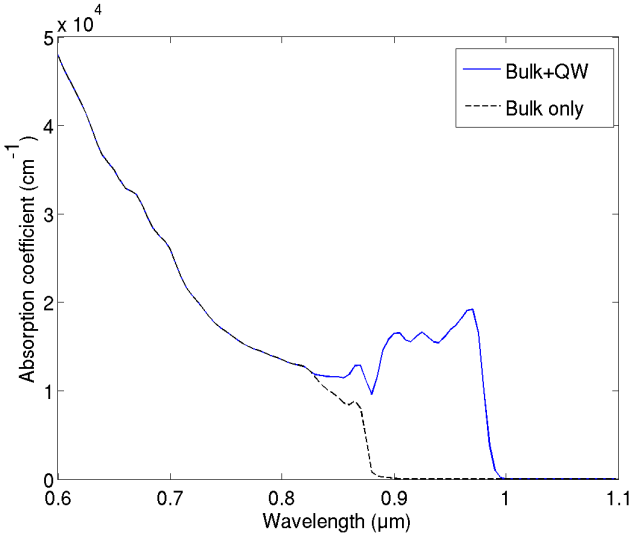

Figure 24: MQW absorption calculated with 8-band k.p including excitonic effects.

The next step is to include this absorption model in the previously developed solar cell model. In strain-compensated QW cells, there is often a thin GaAs layer between the QW and the strain balancing layer in order to improve the quality of the epitaxial growth. As the bandgap of pure GaAs is smaller than the usually high bandgap of strain balancing materials such as GaAsP, a thick interlayer would affect the QW wavefunction and lower the energy level in the QW which would be beneficial for QW solar cells but has to be balanced against the need for a high number of QWs and the potential for coupling between QWs which has similar effects but require small distances between QWs. So far, there haven't been any studies on the influence of the interlayer on the QW properties, so a small study using the above-mentioned 8-band k.p code was performed. The studied structure consists of 7.4 nm $In_{0.23}GaAs$ QW sandwiched between 10.8 nm $GaAs_{0.61}P$ strain compensating barriers, with GaAs interlayers of varying thicknesses added between the QW and the GaAsP layers. ***Figure 24*** shows the impact of the interlayer on the 1st electron level in the QW and its associated absorption coefficient. The effect of the interlayer on holes was found to be insignificant due to the higher effective mass of holes. We see that the shift in electron energy is of the order of 20 meV, which is roughly equivalent to a redshift of 15 nm for a 1.27 eV QW effective bandgap. We also see that the absorption is reduced somewhat,

but not significantly. A series of QWs with different GaAs interlayer thicknesses will be grown to verify these findings.

Optimization of InGaAs QW Growth by MOVPE

A robust simulation methodology for quantum well-enhanced solar cells has been developed using the Crosslight simulation platform. For the initial investigation of the available parameter space, nip polarity GaAs solar cells with various quantum well (QW) configurations were simulated. Three separate designs were analyzed: First, the effect of # of QW layers was investigated using multiple periods (1X, 5X, 10X MQWs) of a 5nm $In_{0.25}Ga_{0.75}As$ QW with a GaAs barrier thickness of 10 nm. Next, the number of periods was fixed and the indium composition was varied. A 10x period MQW was used with 5 nm InGaAs QWs with In compositions ranging from 10% In to 25% In. Finally, the effect of the QW thickness was studied. A 5x $In_{0.25}Ga_{0.75}As$ /GaAs MQW structure was used where the QW thickness was varied from 5 nm to 15 nm.

A single QW results in a sub-band current enhancement of 0.0184 mA/cm^2, which does not show up in AM0 JV results due to minor fluctuations in bulk response. Adding a single QW results in a drop in V_{oc} of 9.9 mV and no apparent current enhancement. Scaling to 5x MQW results in a sub-band current enhancement of 104 µA/cm^2, or a 20.8 µA/cm^2/QW enhancement. Finally, scaling to 10 MQW increases the sub-band current enhancement to 202 µA/cm^2 enhancement, or a 20.2 µA/cm^2/QW which is close to double the current increase from the 5X structure as expected. Therefore, the QWs exhibit the anticipated increase in Jsc. However, a sharp decrease in EQE in the visible spectrum (<700 nm) is observed. The origin of this decrease is unclear at present and further analysis of the Crosslight model is required to pinpoint the source of the discrepancy in the visible spectrum. The shape of the sub-band response also appears much more step-like, while a more excitonic absorption peak is expected.

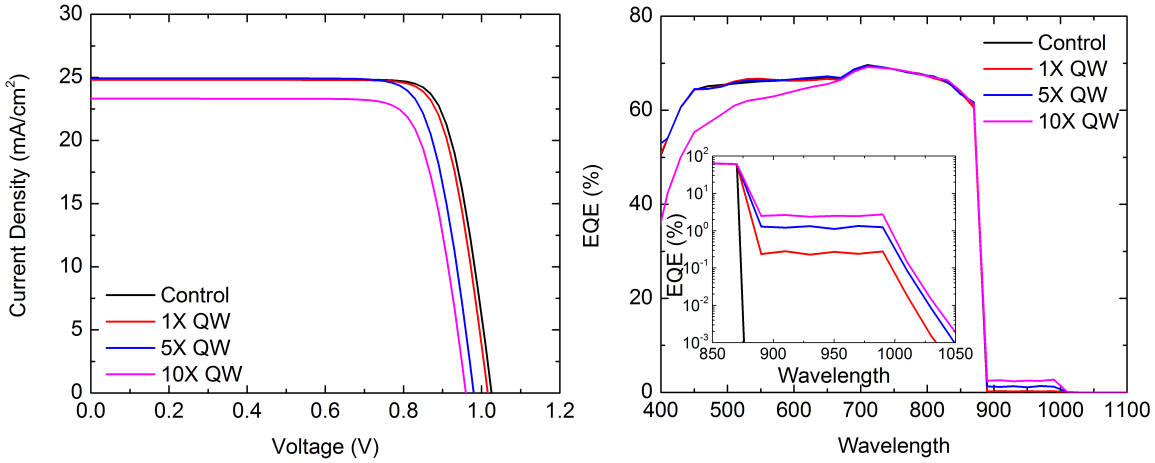

Figure 25: AM0 JV results (left) and EQE results (right) with devices where $In_{0.25}Ga_{0.75}As$ QW thickness is kept at 5nm and stack height is varied from 1X to 10X.

Table 2: Summary of device results when $In_{0.25}Ga_{0.75}As$ QW thickness is kept at 5nm and stack height is varied from 1X to 10X.

Device	Control	1x QW	5x QW	10x QW
Voc	1.0255	1.0156	0.9799	0.9596
Jsc (mA/cm^2)	24.83	24.8	24.93	23.32
Pmax	2.06E+01	2.03E+01	1.94E+01	1.78E+01
FF	81.00%	80.70%	79.50%	79.30%
Efficiency	15.10%	14.90%	14.20%	13.00%
Full Integrated Jsc (mA/cm^2)	25.48	25.49	25.62	24.06
Integrated Jsc Past 870nm (mA/cm^2)	0.3287	0.3471	0.4329	0.5311
Per QW contribution (mA/cm^2)	N/A	0.0184	0.0208	0.0202

*Figure **26*** and *Table **3*** show the results generated when MQW stack height is maintained at 10X, QW thickness is kept at 5 nm, and the In composition is varied. As expected, the absorption edge blueshifts with decreasing In concentration, and V_{oc} is recovered. A high In concentration will present challenges with growth not shown in these simulation due to buildup of strain. All the structures simulated in this sub-study (*Figure **26***) exhibit the same decrease in EQE in the visible region observed for the 10x period in *Figure **25***. Our future plans include identifying whether the simulation is properly modeling QW optical band structure.

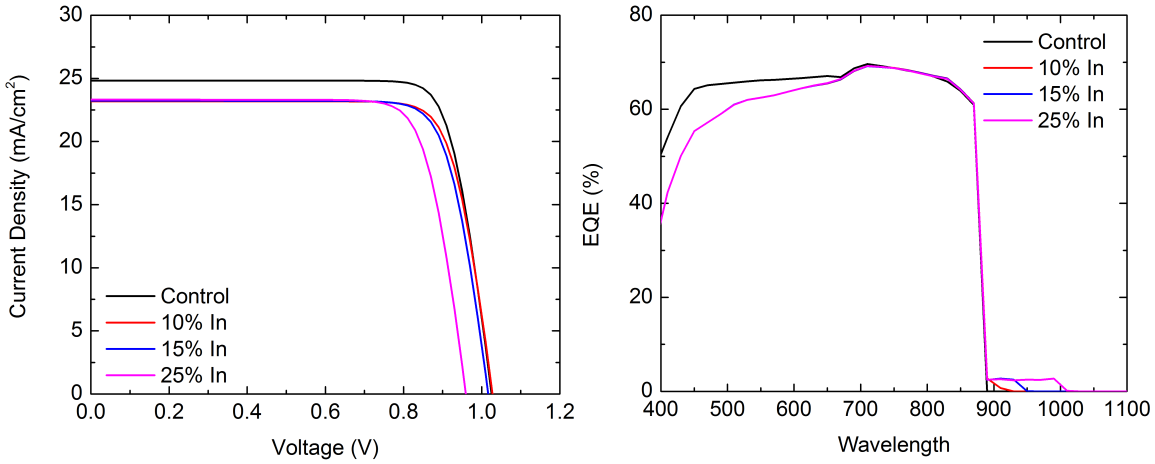

Figure 26: AM0 JV results (left) and EQE results (right) with devices where $In_xGa_{1-x}As$ QW, with x varied from 0.1 to 0.25, thickness fixed 5 nm, and stack height is fixed at 10X. As expected, devices with shallower wells exhibit higher V_{oc} values.

Table 3: Summary of device results when $In_xGa_{1-x}As$ QW, with x varied from 0.1 to 0.25, thickness fixed 5 nm, and stack height is fixed at 10X.

Device	Control	10% In	15% In	25% In
Voc (V)	1.0255	1.0278	1.0168	0.9596
Jsc (mA/cm^2)	24.83	23.19	23.23	23.32
Pmax (mW)	2.06E+01	1.91E+01	1.89E+01	1.78E+01
FF	81.0%	80.1%	80.0%	79.3%
Efficiency	15.10%	14.00%	13.80%	13.00%
Full Integrated Jsc (mA/cm^2)	25.48	23.92	23.97	24.06
Integrated Jsc Past 870nm (mA/cm^2)	0.3287	0.3838	0.4373	0.5311
Per QW contribution (mA/cm^2)	N/A	0.0055	0.0109	0.0202

*Figure **27*** and *Table **4*** show the results of increasing well thickness while keeping In composition fixed at 25% and stacking height at 5X. As shown in *Figure **27*** (right), the collection profile from the QWs starts to take on a slope, more like what is expected from MQWs suggesting that the flat profile with 5 nm wells may be partially caused by a meshing issue in the simulation setup.

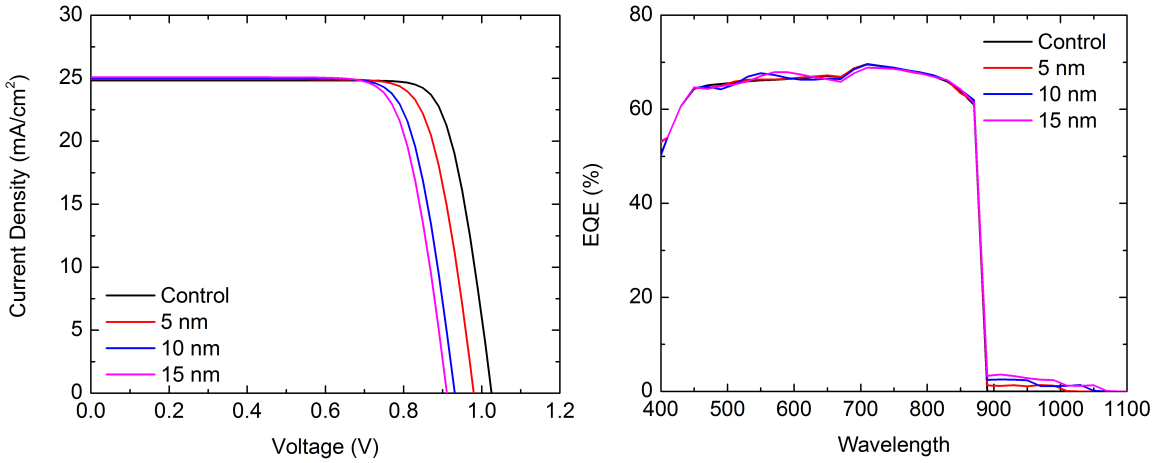

Figure 27: AM0 JV results (left) and EQE results (right) with devices where $In_{0.25}Ga_{0.75}As$ QW thickness is varied from 5 nm to 15 nm and stack height is fixed at 5X.

Table 4. Summary of device results when $In_{0.25}Ga_{0.75}As$ QW thickness is varied from 5 nm to 15 nm and stack height is fixed at 5X.

Device	Control	5 nm Well	10 nm well	15 nm Well
Voc	1.025	0.98	0.931	0.911
Jsc (mA/cm^2)	24.83	24.93	25	25.08
Pmax	2.06E+01	1.94E+01	1.83E+01	1.79E+01
FF	81.00%	79.50%	78.70%	78.30%
Efficiency	15.10%	14.20%	13.40%	13.10%
Full Integrated Jsc (mA/cm^2)	25.48	25.62	25.69	25.80
Integrated Jsc Past 870nm (mA/cm^2)	0.3287	0.4329	0.5281	0.612
Per QW contribution (mA/cm^2)	N/A	0.0208	0.0399	0.0567

*Figure **28*** presents a graphical summary of the simulation results. It is important to note that the devices that were part of the In composition study all suffered from decreased short wavelength response from the 10X QW stack height. Moving forward, the model will be improved upon to provide more accurate results, and an in-house QW absorption and minority drift-diffusion equations will be developed in-house as a basis for comparison.

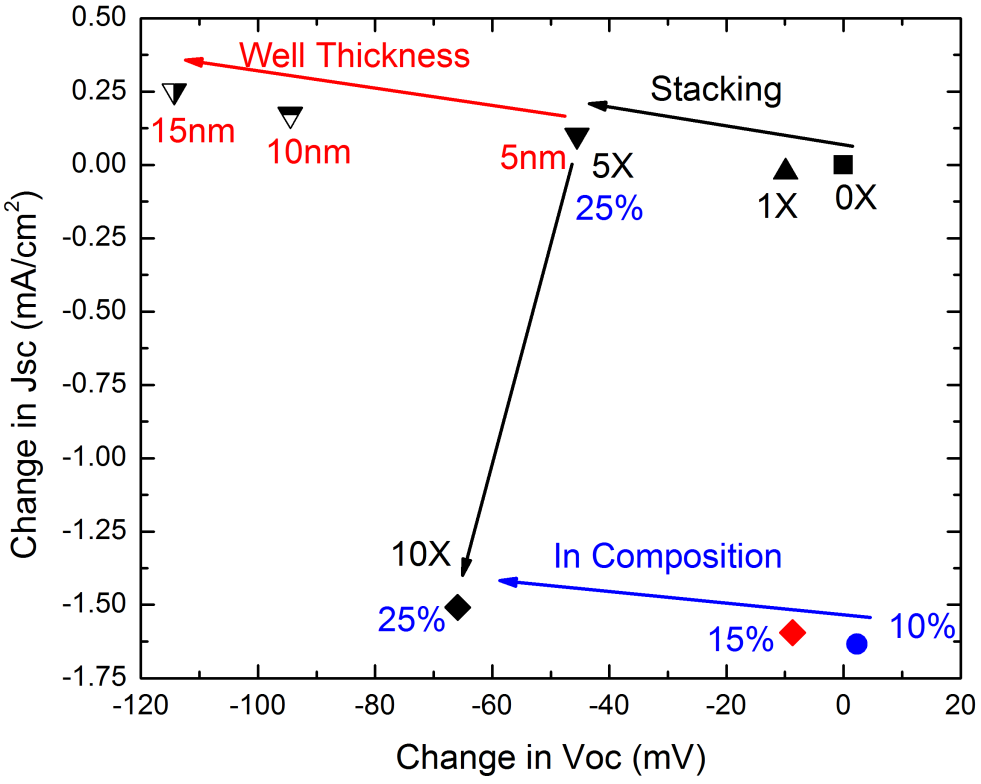

Figure 28: Summary of results plotted as change in J_{sc} vs change in V_{oc}.

Growth of Baseline, QW and QD Solar Cells

The use of nanostructures such as quantum dots (QD) offers tremendous potential to realize high-efficiency photovoltaic (PV) cells. The optimization of the electronic structure of the layers within the QD region should lead to improved PV performance. This includes the QD layer itself, but also the surrounding barrier and/or strain balancing layers that comprise the QD active region. In this paper, the effect of the GaAs capping layer thickness (i.e. the first layer grown following QD) on the optoelectronic properties of InAs QDs was investigated. The GaAs capping layer plays a crucial role in the physical and optoelectronic properties of the QD. The GaAs capping thickness strongly modifies the InAs QD wavelength and also enhances the QD emission relative to the wetting layer (WL) emission. This behavior implies a suppression of WL emission that is thought to be a drawback to high-efficiency photovoltaic performance. In the final paper, we investigate how this WL PL-suppression affects the performance of QD-enhanced GaAs single junction solar cell performance.

Introducing quantum dots (QD) in GaAs solar cells has been shown to increase current densities but is often associated with a decrease in voltage. By δ-doping the QDs, the confined states in the QDs become partially filled which can lead to an increase in sub-gap collection. This doping also flattens the band structure near the QDs and reduces the non-radiative recombination of confined carriers, resulting in less voltage loss under illumination and larger luminescence under injection. These conditions lead to an overall more efficient QD solar cell through the use of δ-doping.

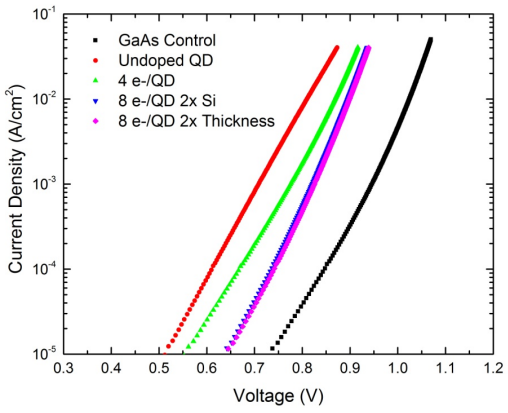

Sample	I_0 (A/cm^2)	Ideality Factor
GaAs Control	1.13×10^{-18}	1.08
Undoped QD	1.89×10^{-10}	1.77
4 e-/QD	9.19×10^{-13}	1.45
8 e-/QD 2x Si	2.86×10^{-15}	1.20
8 e-/QD 2x Thickness	1.64×10^{-15}	1.19

Figure 29: I_{SC}-V_{OC} results of doped QD cells compared to undoped and control devices.

Growth and characterization of QD based solar cells using improved uniformity QD growth recipes

A 5-period superlattice was grown consisting of repeating layers of InAs QD, a LT-GaAs capping layer, a HT-GaAs spacer layer, a GaP strain-balancing layer and a final GaAs spacer

layer. LT and HT refer to low and high temperature respectively and it is the LT-GaAs layer thickness that is varied in this study. The InAs QD are formed by the strain-driven Stranski-Krastanow growth mode and are grown at 485°C. The InAs coverage was nominally 1.8 ML for all samples. A 60-second H2 growth interrupt is used to facilitate QD formation followed by the LT-GaAs cap layer. The LT-GaAs thickness was varied between 1.0 and 4.0 nm. Following the LT-GaAs cap layer, the temperature was increased to 590°C for the balance of the structure. After the 5-period QD superlattice, a 33 nm GaAs spacer layer was grown followed by a surface layer of InAs QDs grown under identical conditions as in the structure.

A wavelength redshift can be seen for the QD PL emission illustrated in ***Figure 30*** as a function of LT-GaAs cap thickness. For a fixed nominal coverage of InAs, the QDs that are formed following a 60 second GRI exhibit similar size and diameter distributions. When the LT-GaAs cap layer is thinner than the QD height, then any exposed InAs either evaporates or surface diffuses away. In this manner, a thinner LT-GaAs would result in shorter average height QDs, and therefore a shorter wavelength. As the LT-GaAs cap thickness increases, the average QD height increases leading to a net redshift in emission.

The saturation in redshift can be explained by considering that the average height of as-deposited QDs is on the order of 2-3 nm as determined by AFM measurements. For LT-GaAs cap thickness of this magnitude the QDs are fully capped and are no longer changing their size. Therefore, less wavelength shift is expected for a thicker LT-GaAs cap.

The increase in intensity indicates that more carriers are recombining in the QD as the LT-GaAs increases. Due to the physical proximity of the WL and QD, there will be a competition between excited carriers recombining in either the WL or the QD. Due to the spatial distribution of the QD, there are regions where recombination will occur in the WL despite the higher energy of that transition. For thin LT-GaAs capping, the overall volume of QD is reduced due to the thickness reduction which contributes to reduced PL intensity. As the QD thickness increases, due to increased LT-GaAs cap thickness, the QD have a larger capture volume for carriers as well as better confined, deeper quantum states. Other studies that intentionally increase the InAs thickness through deposition time also exhibit this shift from WL dominant PL to QD-dominant PL.[1] The temperature dependent PL results will provide insight into the recombination processes for both the WL and QD.

This approach of controlling the QD height using the LT-GaAs cap instead of InAs coverage should reduce the problems observed with coalescence of QDs at higher InAs coverage values. The reduction in coalescence is a key factor in improving Voc in QD-enhanced solar cells.[2, 3]

Subsequent work explores the effect of modification of the QD stack has on the AM0 response of 10-period InAs QD-enhanced GaAs solar cells as a function of the LT-GaAs thickness. It is anticipated that the Voc will be the most significant change as function of capping thickness.

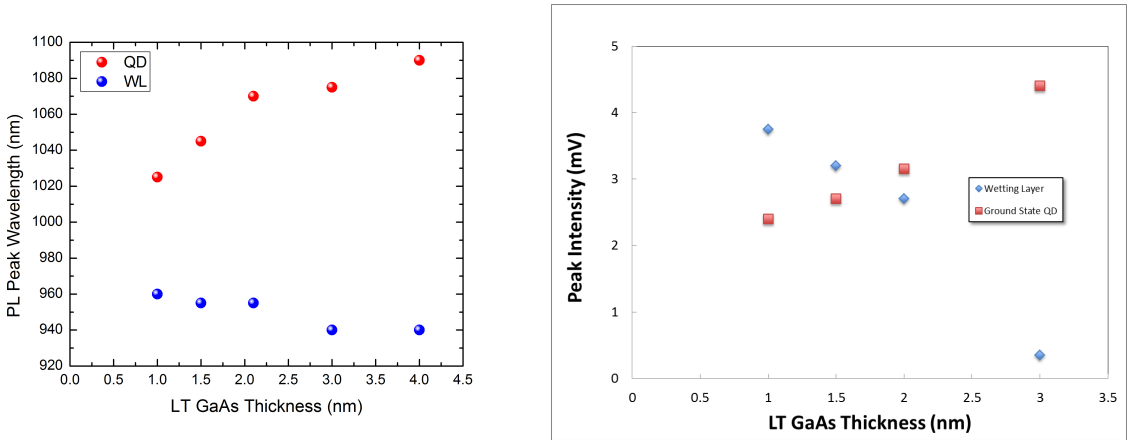

Figure 30: PL wavelength as a function of LT-GaAs thickness for WL and QD. Peak PL intensity as a function of LT-GaAs thickness.

Growth of a Series of QD Cells using Various Levels of Si δ-doping in the i-region

Further improvements in sub-gap collection efficiency may be possible by the addition of δ-doping, which provides carriers to partially fill the confined states in the QDs ensuring carriers are more readily available for transitions into conduction band states by low energy photons. Devices incorporating QDs substituted a portion of the i-region with ten repeat units of a periodic structure consisting of the InAs QDs, followed by a low temperature GaAs cap, a high temperature GaAs spacer, a GaP strain compensation layer (SCL), and a final high temperature GaAs spacer. To δ-dope the structure, a layer of Si-doped GaAs replaced a section of the first high temperature GaAs spacer. The thickness of this doped layer was chosen to achieve an areal doping of 4 or 8 electrons per quantum dot (4e-/QD, 8e-/QD), based on measured QD areal density of approximately 5x1010 cm-2. Two methods were used to obtain 8e-/QD, one where the silane flow was increased by a factor of two to double the doping of the 4e-/QD design (2x Si), and the other was to leave the doping level the same and double the thickness of the Si-doped layer, while further reducing the high-temp GaAs spacer layer (2x Thick).

External quantum efficiency analysis of the sample set reveals small differences between doped and undoped devices. ***Figure 31*** shows an enlargement of the sub-bandgap absorption of the QD devices as compared to a GaAs control. These data were integrated against AM0, which is shown in the table. All devices incorporating quantum dots show improved current density over the GaAs control, but all devices perform nearly identically sub-GaAs bandgap. Improvement is seen in doped QDs beyond 1050 nm over the undoped sample. Similar changes were seen in photoluminescence (PL) measurements.

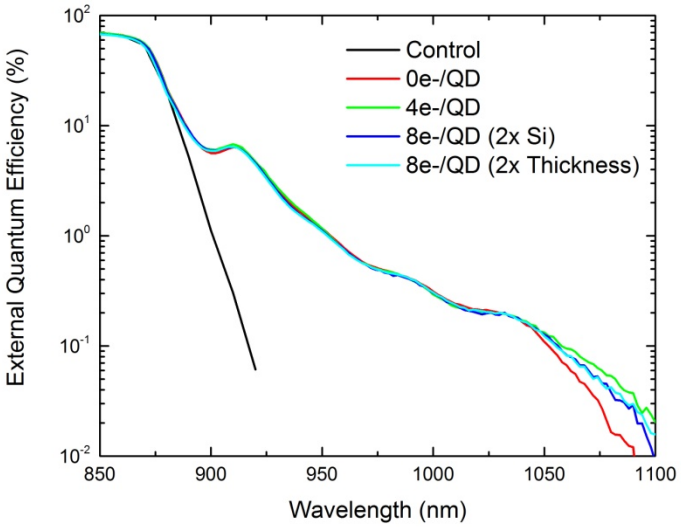

TABLE I
INTEGRATED AM0 CURRENT DENSITIES

Sample	Integrated Jsc (mA/cm^2)	Integrated Sub-Gap Jsc (mA/cm^2)
GaAs Control	22.97	0.079
Undoped QD	23.62	0.291
4 e-/QD	23.76	0.298
8 e-/QD 2x Si	23.45	0.289
8 e-/QD 2x Thickness	23.37	0.281

Figure 31: Sub-gap external quantum efficiencies of δ doped QD devices and table showing integrated AM0 current densities

Figure ***32*** shows PL spectra of all samples. Each device shows a strong luminescence peak near 1042 nm, while doped QDs also exhibit a stronger peak at 1074 nm. This lower energy transition exists in the undoped QD sample but is not nearly as strong.

Ground state recombination may exhibit a non-negligible SRH mode, where radiative recombination is quenched by non-radiative recombination events. As the QDs are doped, the band structure around the QDs is flattened and changes the location of the Fermi level relative to the conduction band, moving it away from midgap. By flattening the bands, the dominant SRH recombination zone is pushed towards the p-type emitter away from the QDs. Similar results have been observed by simply changing the location of QDs within the intrinsic region. When QDs are in the center of the i-region, the higher energy peak dominates PL, while QDs close to either the emitter or the base exhibit a stronger lower energy peak.

AM0 characterization revealed additional differences in the samples. J_{SC} between the devices was statistically similar, but V_{OC} from doped QDs was enhanced over undoped dots. At 4e-/QD, the V_{OC} was improved 63 mV on average over the undoped QDs, while the increased 8e-/QD doping furthered this increase to 71 mV. A similar trend was seen in fill factor and conversion efficiency, resulting in average absolute efficiency increases of 1.29% and 1.43%, respectively, over the undoped QD cells.

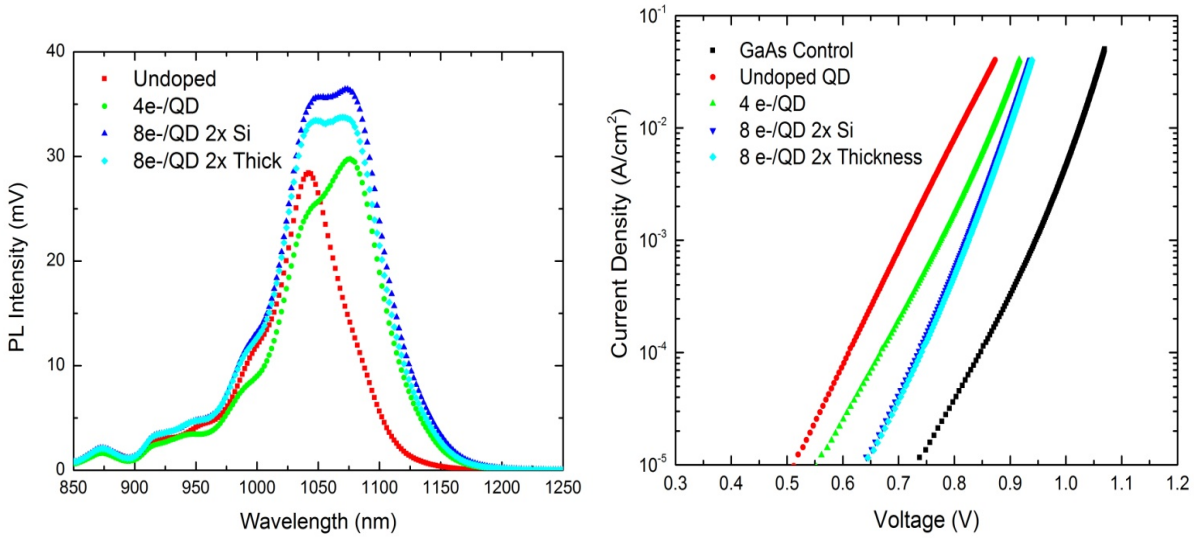

Figure 32

ISC-VOC measurements, taken up to current densities of approximately 2-suns, show the source of the voltage improvements. These data were fit using a standard single diode model about the 1-sun current density. As seen in ***Figure 32***, the dark current of the cells decreases towards the levels of the control as doping is introduced and increased. Additionally, the ideality factor decreases as dopant is added.

This result further elucidates the effects of band bending from the Si dopant. The flattened bands exhibit more quasi-neutral-region-like recombination (ideality factor = 1), reducing overall recombination current and increasing voltage.

In the next quarter, a wider range of doping levels will be examined to explore the limits of improvement. Additionally, low temperature measurements of SR under voltage and light bias will be used to explore the fundamental carrier escape mechanisms of these doped quantum dots, which can be by a two photon process, phonon-assisted process, or tunneling escape. Finally, photoreflectiance will be used to analyze the built in field of these sample, and explore the interband transitions of the quantum dot states.

Growth and Characterization of QD Based Solar Cells using Improved Uniformity QD Growth Recipes

As previously discussed, both 2° and 6° degree offcut samples support QD solar cells as long as the change in QD critical thickness is accounted for. Continuing the study into effects of vicinal offcut to improve QD density and quality, we have grown 5-layer InAs QD test structures on 2° samples offcut to our previous standard direction (<110>) as well as toward the <111>B direction. The effects of offcut direction are changes in the surface step edge, from a zigzap like structure comprised of [110] facets to a straight line structure terminated by As atoms. Effects of QD growth rate and V/III ratio were also studies. AFM images for this study are shown below as well as average QD height, diameter and density and the photoluminescence spectra.

The samples to the left are grown with our standard conditions of 1.8ML of InAs at 0.14 ML/sec, a V/III of 12 and T_g of 470°C. As can be seen, the QD align along the step edge in both <110> and <111> cases, QD size and density remain very similar. However, the photoluminescence (PL) QD ground state peak at 1100nm is reduced by ~3 times. This may be an indication of increased non-radiative recombination rate in the <111> sample, perhaps due to defects in the QD, although further examination of this sample is required.

In the middle plots, the InAs QD growth rate was doubles while the growth time as halved. Results clearly show that increasing the growth rate leads to overall larger QD and perhaps increased QD coalescence. This result shows that both the total amount as well as the flux of Indium is important in determining QD size and density. However, the PL results for this sample do not show a shift in QD ground state wavelength or intensity compared with the standard sample. This may indicate that in both samples, only a portion of the smallest QD are actually emitting light. As well, the capping procedure may be critical in determining the "buried" QD size and density. Further tests are planned to explore effects of capping layer on QD PL.

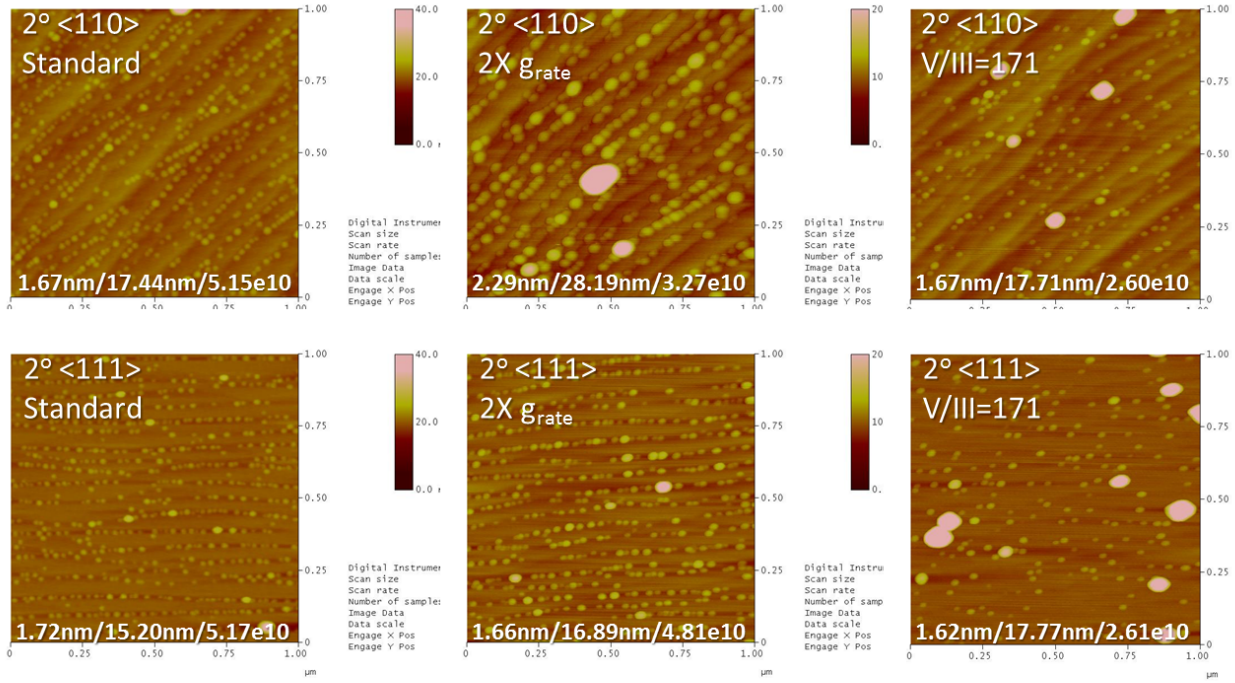

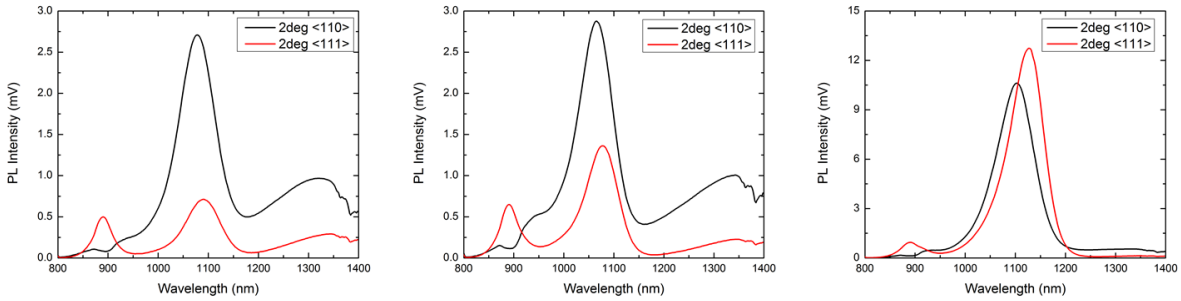

Figure 33: Atomic force micrographs for both the <110> and <111> offcut substrates as a function of growth conditions. The numbers at the bottom of the figure show QD height, diameter and density. At the bottom of each column, the PL spectra for each growth condition are shown. The QD ground state peak is near 1100 nm in all cases.

Finally, by increasing the V/III ratio to 171 (right samples) as compared to our standard, QD size is relatively unaffected, but density is reduced by ~2 times. As well, QD coalescence is enhanced leading to a higher density of large coalesced QDs. This effect may be related to the dramatic changes in viscosity of the gas mixture, since the V/III is changed only by increasing the arsine flow. Higher gas viscosities can impede QD nucleation as well as enhance the ripening process. On the other hand, the PL shows a dramatic increase in QD ground state peak intensity is actually enhanced by a factor of 3 for the <110> offcut direction and a factor of 12 for the <111> direction. Thus, despite the reduction in QD density and increased in coalesced QD, the total radiative emission rate is in fact improved at high V/III ratio. This fact may translate to improved absorption in QD solar cells.

Our next tasks will but to study the effects of zero degree offcut on QD growth and nucleation. QD based solar cells will be grown and tested under various QD growth conditions such as zero offcut and high vs. low V/III ratio.

Simulation and Modeling of Baseline and QD Cells using Crosslight

The physics-based software Crosslight APSYS has been developed to investigate the design parameters of QD enhanced solar cells with particular focus on the InAs/GaAs system. This methodology is used to study how nanoscale variables, including size, shape and material compositions, influence photovoltaic performance. In addition, device-level engineering of the nanostructures is explored in optimizing the overall device response. Specifically, the effect of the position of the QDs within the intrinsic regions was investigated. Preliminary simulations suggest strategically placing the QDs off-center reduces non-radiative recombination and thereby the dark saturation current, contributing to a marked increase in open- circuit voltage and fill factor. The short-circuit current remains unchanged in the high field region resulting in an increase in overall conversion efficiency. To further explore this finding, a series of three samples with the QDs placed in the center and near the doped regions of a pin-GaAs solar cell have been grown using MOCVD, fabricated and fully characterized (see ***Figure 34***). Contrary to predictions, the emitter-shifted devices exhibit a marked decrease in open-circuit voltage and fill factor. This behavior is attributed to non-negligible n-type background doping in the intrinsic

region, which shifts the region of maximum recombination towards the p-type emitter (***Figure 35***).

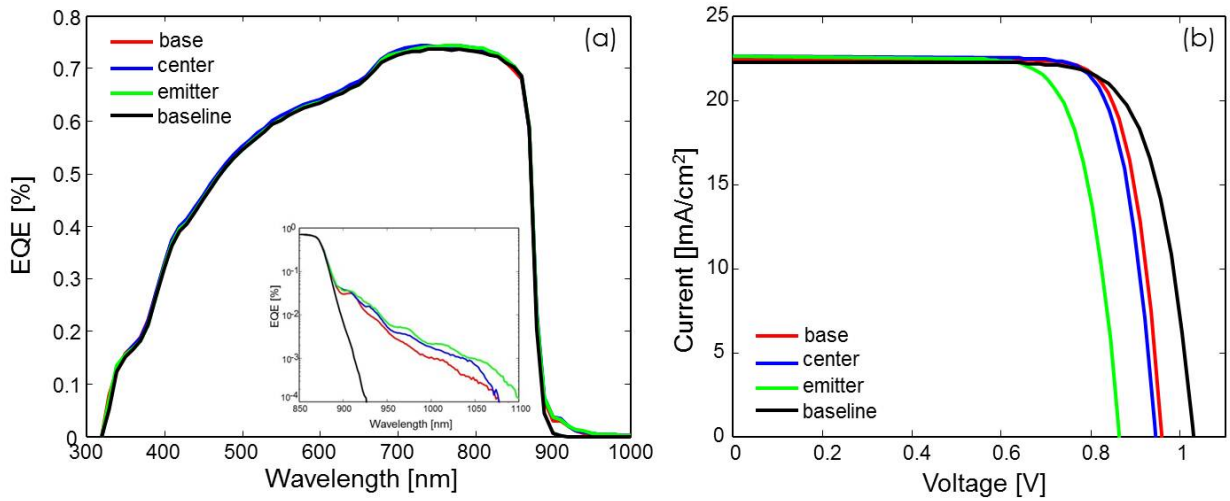

Figure 34: Measured (a) external quantum efficiency versus wavelength (b) current-voltage characteristics for baseline and QD-enhanced pin-GaAs solar cells. The inset highlights the sub-bandgap photoresponse due to absorption by the quantum dot superlattice.

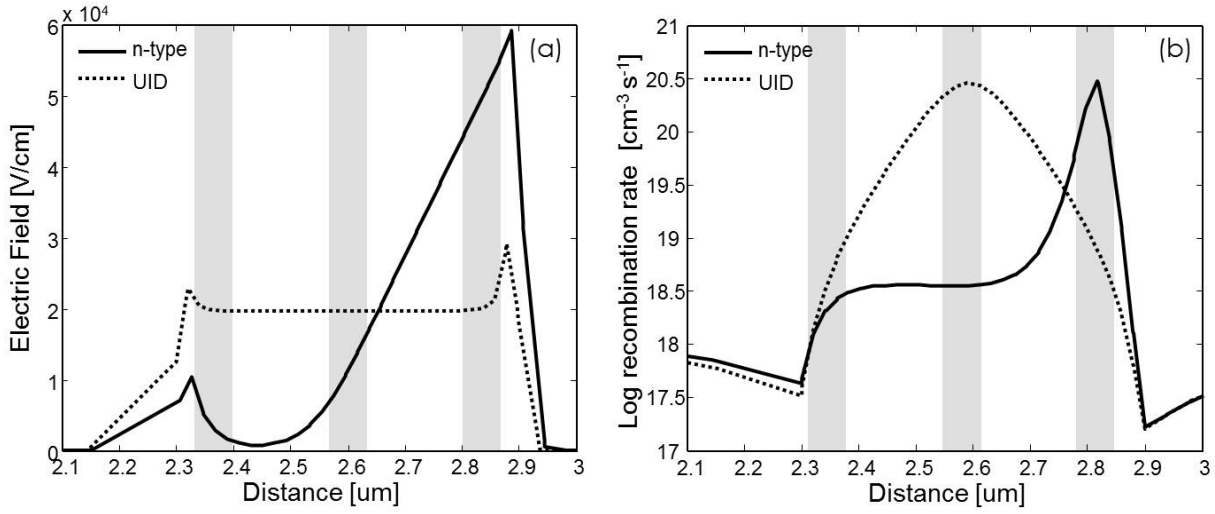

Figure 35: Simulated (a) electric field and (b) SRH recombination rates versus position for an n unintentionally doped and ~1 x1016 cm-3 n-type intrinsic region. The shaded regions correspond to the position of the QDs in the base-shifted, centered and emitter-shifted devices.

Necessary to the optimization process of this particular class of solar cells is the ability to correlate nanoscale properties with macroscopic device characteristics. To this purpose, we have developed a modeling routine using the physics based software Crosslight APSYS to systematically study how the inclusion of embedded quantum structures influence the performance of photovoltaics. Crosslight APSYS is a general purpose 2D finite-element analysis and modeling software program designed for compound semiconductor devices based

on the drift-diffusion model. In addition, and unique to this platform, is the ability to model quantum confinement effects (which arise when nanoscale layers are implemented) with an intrinsic Schrödinger solver. In particular, this tool is applied to study how nanoscale variables, including size, shape and material compositions, alter the electrical and optical properties at the device level. In addition, macro-level engineering of the nanostructures, such as the number of stacked layers as well as the position of these structures within the device, can be explored in optimizing the overall device response.

As a preliminary step, the program was used to predict the performance of a single-junction *pin*-GaAs solar cell which will serve as the baseline for subsequent studies. As shown in ***Figure 36***, the simulation results agree well with measured data from an actual device with calculated values for V_{OC}, J_{SC}, fill factor and power conversion efficiency of 1.034 V, 22.49 mA/cm^2, 80.12% and 13.64%, respectively and include all major loss mechanisms including spectral reflection and carrier recombination. The material parameters employed are taken from widely accepted databases based on measurements and physical models. It is worth noting that no anti-reflection coatings were used in order to focus solely on the change in device performance due to the embedded nanostructures.

In parallel, the quantum module was used to calculate the band structure and absorption of a multi-layer stack of InAs QDs embedded in GaAs. For this investigation a truncated pyramid with a height (base) of 3.5 nm (20 nm) was selected to best describe the physical system. In addition, a thin layer of InGaAs (0.5 nm) has been included in the quantum solver to take into account absorption due to wetting layer states and a QD surface density of $1x10^{10}cm^{-2}$ assumed. Within the software it is possible to incorporate the outputs of the quantum solver, including bound energy state levels and optical transition strengths, as parameters of the active region of the device. This technique enables full characterization of the nanostructured device and has been used to explore a range of devices with various geometries.

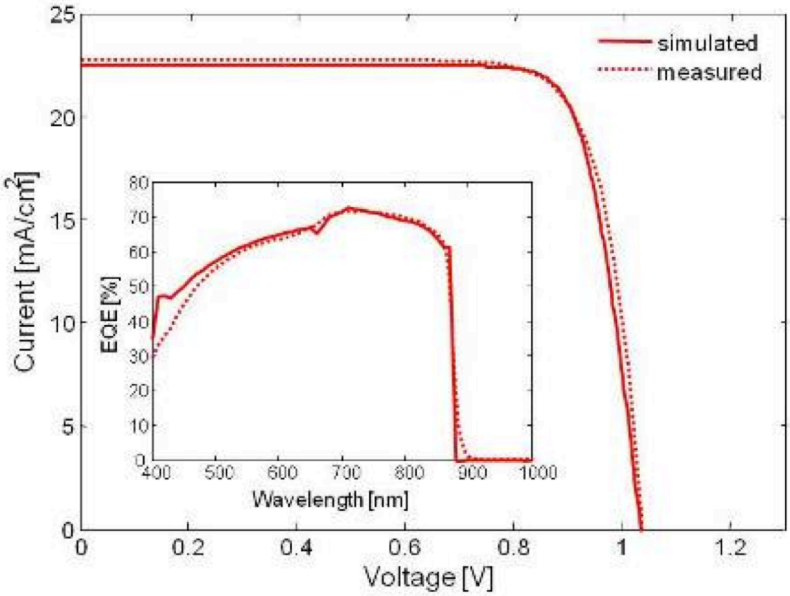

Figure 36: Simulated (solid) and measured (dotted) current-voltage characteristics for a pin-GaAs solar cell. The inset shows the external quantum efficiency spectra.

The simulation results based upon the two-step process described are depicted in ***Figure 37*** for a baseline and a nanostructured *pin*-GaAs solar cell. In this case, a 5 layer superlattice of uncoupled InAs QDs was centered in the intrinsic region of a *pin*-GaAs cell. For comparison, the active region in both devices was kept constant at 100 nm and all simulations were performed under AM0 conditions. The enhancement in performance offered by the incorporation of QDs is clearly visible in the external quantum efficiency spectrum where sub-bandgap absorption is observed at wavelengths above 880 nm. Two prominent peaks predicted at 940 and 1060 nm can be ascribed to transitions between confined stated of the wetting layer and QD, respectively. Based upon the integrated quantum efficiency above 880 nm, our model predicts a short-circuit current enhancement of 0.072 mA/cm^2.

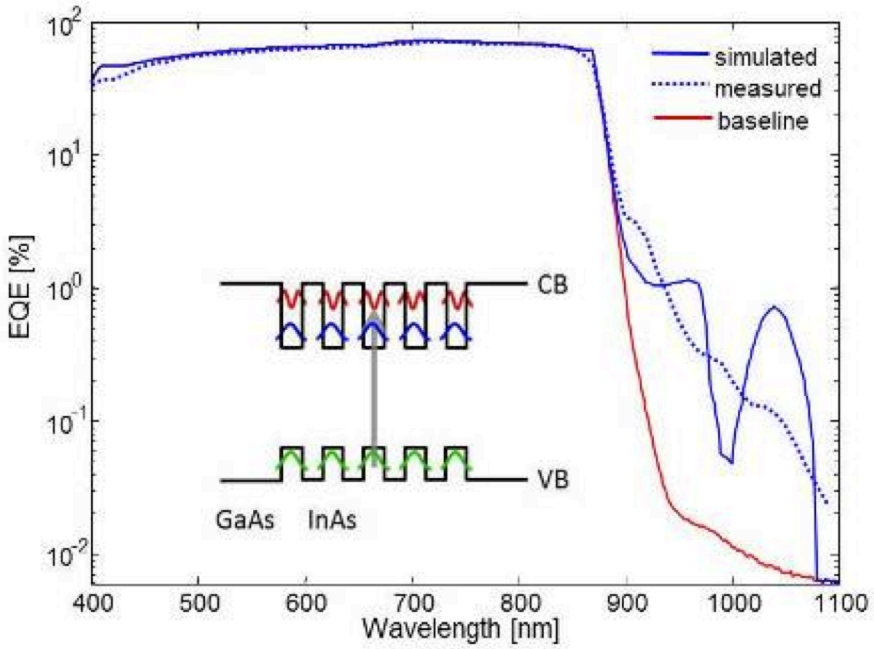

Figure 37: External quantum efficiency versus wavelength simulated for a pin-GaAs solar cell with (blue) and without (red) quantum dots. For comparison representative data from a nanostructured device is also included (blue dotted). The inset depicts the electronic structure of a GaAs solar cell embedded with InAs quantum dots.

For comparison, representative data from a previously fabricated 5-layer QD solar cell is also included in ***Figure 37***, which shows a reasonable correlation between the simulated and experimental results. Here, the integrated measured spectral response above 880 nm yields a 0.092 mA/cm^2 increase in photocurrent. While this is fairly close to the simulation prediction, the discrepancies likely originate from the evident mismatch between the quantum efficiencies observed and predicted. For example, the model simultaneously overestimates the contribution from the QD and underestimates the influence of the wetting layer. In addition there is a notable shift in where these features lie spectrally. As this sub-bandgap contribution to the photocurrent is directly related to the electronic structure of the embedded QDs, it is clear that the quantum model must be further modified to ensure a more accurate representation. One possible source of error is the calculation of the strain distribution within the nanostructure which greatly affects band offsets and confined state levels through the deformation potential. The current software neglects the three-dimensional nature of the strain distribution which gives rise to these discrepancies in transition energies. Although this approach remains suitable for the purpose of predicting trends at the device level, efforts are underway to improve the accuracy of the quantum model using external software such as *nextnano*[3].

Simulation and Device Design of InGaP-GaAs Hetrojunction Solar Cells

Previous nip and heterojunction QDSCs exhibited a degraded bulk spectral responsivity due to emitter degradation not seen in the standard pin control cell. This was attributed to short minority carrier diffusion length in n^+ GaAs and InGaP. A study was performed to assess the effects of

thinning the cell emitter in order to reduce absorption and enhance carrier collection in the heavily-doped emitter. A 31 mV reduction in V_{oc} was seen with the 30 nm emitter heterojunction design, but a 950 µA enhancement was measured in short circuit current density, and a slightly improved fill factor was measured. This resulted in an absolute efficiency improvement of 0.4% with the heterojunction design. The next step in this study is to regrow QDSCs using the 50 nm nip and 20 nm InGaP heterojunction cell design.

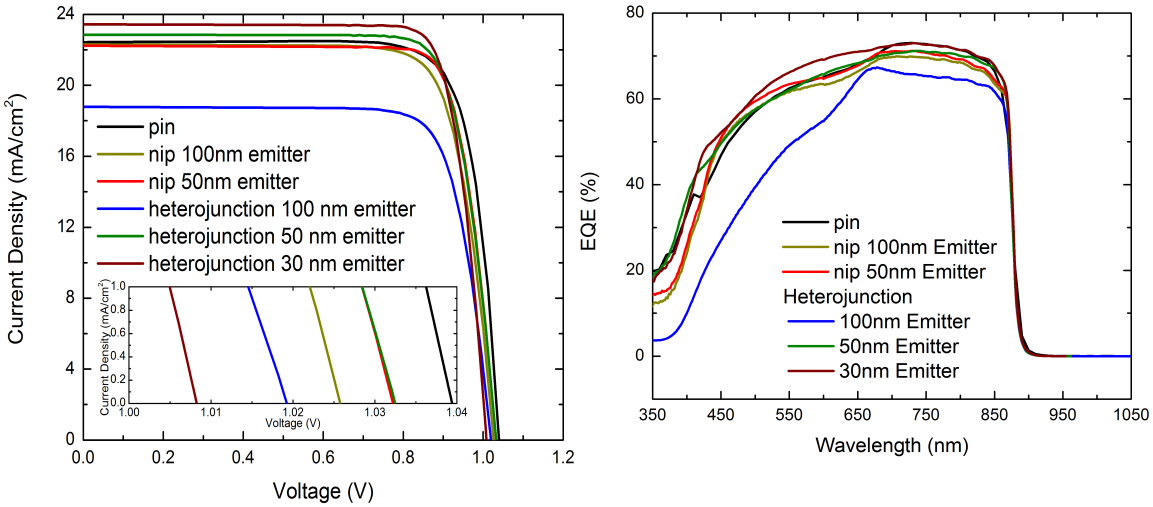

Figure 38: One sun AM0 current-voltage curves and external quantum efficiency for the homojunction pin and nip cells as well as the various heterojunction designs.

Table 5: Solar cell results under one sun AM0 illumination.

Device	J_{sc} (mA/cm^2)	V_{oc} (V)	Fill Factor	Efficiency
***pin* Control**	22.47	1.039	80.0%	13.8%
***nip* 100nm Emitter**	22.32	1.025	78.7%	13.3%
***nip* 50nm Emitter**	22.25	1.032	81.4%	13.7%
heterojunction 100nm emitter	18.81	1.020	78.9%	11.1%
heterojunction 50nm emitter	22.88	1.032	80.2%	13.9%
heterojunction 30nm emitter	23.42	1.008	82.3%	14.2%

Growth of a Series of QD cells using Various Levels of Si delta-doping in the i-region

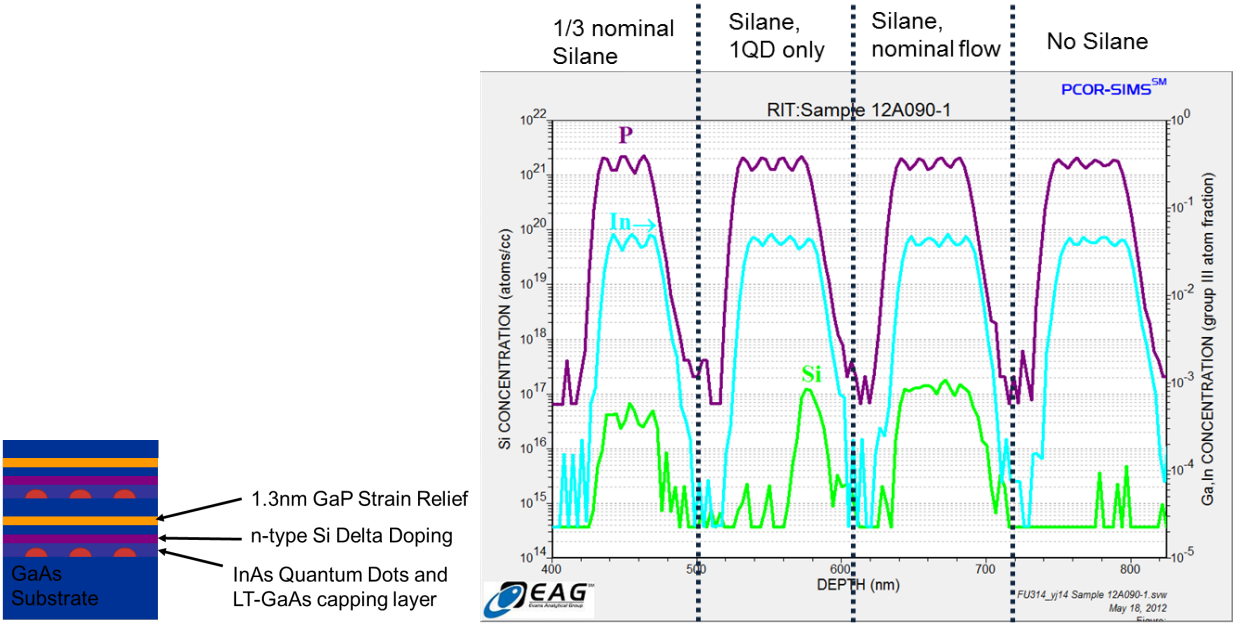

Figure 39: Design of the delta-doping test structure and SIMS results for various silence flows. Both the Si, In and P are plotted, corresponding to the InAs QDs, the GaP strain balancing and the Si delta doping.

In order to calibrate the MOCVD reactor, a test structure was grown with δ-doping in high temp GaAs directly after capping QDs. The bulk doping of this layer was set at 1×10^{17} cm^{-3} over a 2nm layer, giving a δ-doping corresponding to 4 electrons per QD. SIMS results were used to verify ability so control doping in the layer above the QD. As shown in the figure, there is a clear ability to dope QDs, to control the level of doping, and to control which QDs are doped. At this point, several full cells have been grown and are currently in fabrication, these include:

- Baseline 10xQD, no doping,
- 10x QD, 4e-/QD,
- 10x QD, 8e-/QD (thickness increase), and
- 10x QD, 8e-/QD (doping increase).

Improving QD absorption

Solar cells with 10, 20, and 40 layers of QDs have been grown using the optimized InAs surface coverage as described in Phase 1 (pre go/no-go). The 10 and 20 layer devices have demonstrated improved current generation over baseline devices without QDs, as well as comparable current gain from integrated QD response to the non-optimized InAs coverage. The improved InAs coverage has also lead to a continued increase in open circuit voltage as compared to the non-

optimized InAs coverage devices. One sun light IV as well as spectral responses are shown below in *Figure **40***.

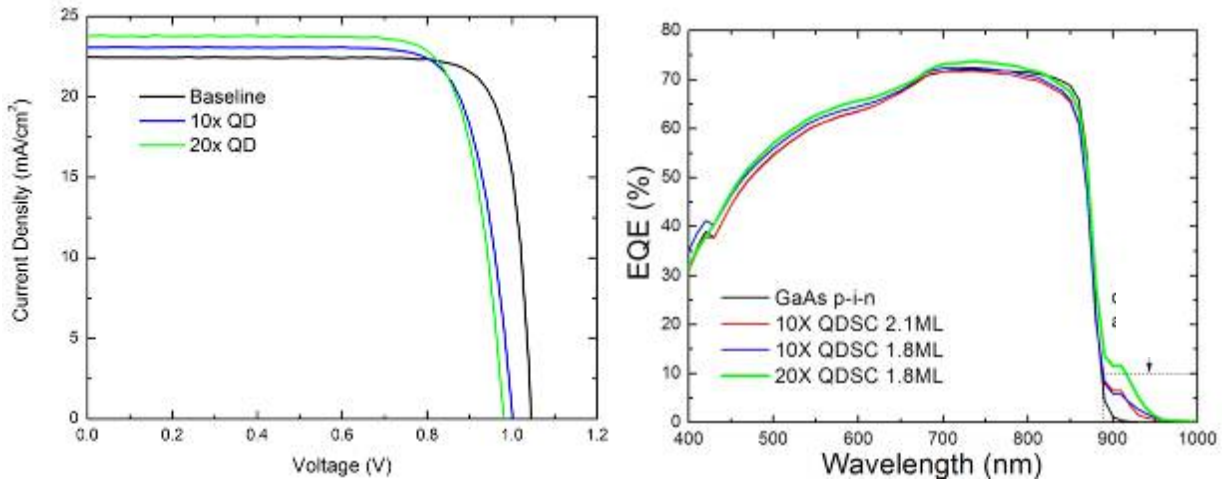

Figure 40: a) One sun light IV for baseline and 10-20 layer QD solar cells b) externals quantum efficiency show the sub-bandgap response region.

Ten, twenty, and forty-layer InAs/GaAs quantum dot (QD) embedded superlattice solar cells were compared to a baseline GaAs *p-i-n* solar cell. Proper strain balancing and a reduction of InAs coverage value in the superlattice region of the QD embedded devices enabled the systematic increase in short circuit current density (see *Figure **41***) with QD layers (0.02 mA/cm^2/QD layer) with minimal open circuit voltage loss (~50 mV). The improvement in voltage was found to be due to a reduced non-radiative recombination resulting from a reduced density of larger defective QDs and effective strain management. The forty layer device exceeded the baseline GaAs cell by 0.5% absolute efficiency improving efficiency relative to the baseline by 3.6%. Results have been reported in two recent publication in the Applied Physics Letters as well as the IEEE Journal of Photovoltaics.

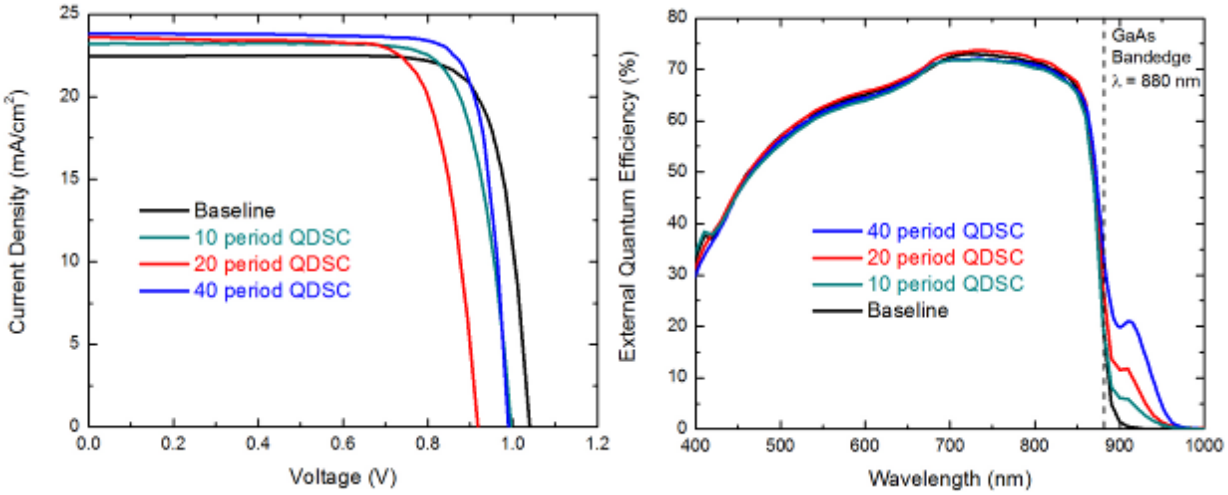

Figure 41: a) Illuminated 1-sun J-V curves for the three QD and the baseline/control GaAs p-i-n solar cell devices, indicating a clear increase in short circuit current density and minimal loss in open circuit voltage for the 10- and 40-layer QD cells. b) External quantum efficiency measurements for the three QD and the baseline/control GaAs p-i-n solar cell devices, indicating no significant degradation in the bulk GaAs absorption wavelengths and a consistent increase in sub-GaAs bandedge EQE values with increasing numbers of QD layers.

Life Cycle Assessment of Organic Photovoltaics

The primary goal of life cycle assessment is to compute the CED of various organic photovoltaic technologies, including single junction small molecule and polymer photovoltaics as well as the multi-junction counterparts, which are responsible for the rapid increase in device efficiency. A secondary goal is to examine the effect of specific processing conditions such as the use of thermal treatment, interface layers, low bandgap polymer and the type of heterojunction approach. The functional unit of this study is the CED to produce a power of 1 watt-peak (CED/Wp). As illustrated in *Figure **42***, the substrate (ITO coated PET), the silver contact and encapsulation constitute the background system. The focus of this work is the material used in the active and interface layers as well as the process energy associated with the deposition and annealing of those layers. Devices illustrated in *Figure **42***, represent the most complex case, where interfacial layers are used in between each active layer. Two types of interfacial layers are used: the electron blocking layer (EBL) and the hole blocking layer (HBL). There is one active layer for polymer photovoltaics but in the case of small molecules, the active layer is actually made of multiple layers combining either a planar or planar-mixed heterojunction.

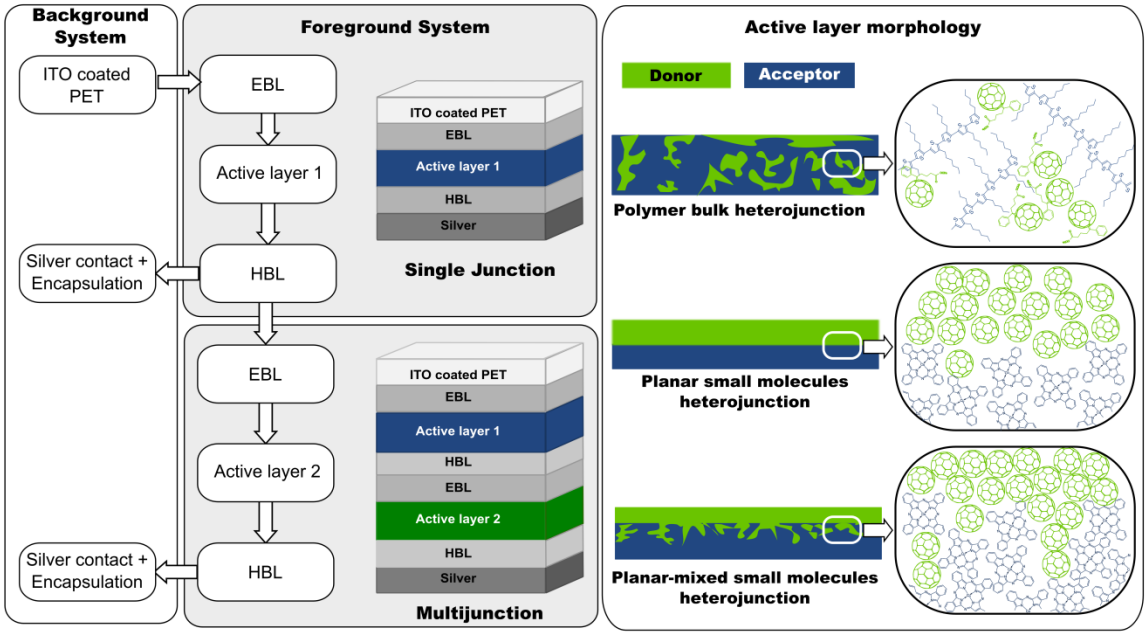

Figure 42: Overview of the process flow for the production of organic photovoltaics and active layer morphologies for polymer and small molecule photovoltaics.

Organic photovoltaics are made of high purity materials which are often recently synthesized (e.g. nanomaterials, novel absorbing dye conjugates, and block co-polymers) and therefore there is no life cycle inventory data available. Therefore, the first step is to calculate the embodied energy of the individual materials on a gravimetric basis using life cycle assessment from cradle to gate. In general, OPV materials fall into 3 categories: electron accepter (e.g. modified fullerenes), donor (polymer and small molecule), and interfacial materials (HBL and EBL). Fullerenes are the most common acceptor material and are used directly with small molecules or after functionalization for improved solubility in polymer photovoltaics. The embodied energy of fullerene production was previously calculated[5] and will be included in the present work. In addition to methanofullerene derivatives (PCBM and *bis*-PCBM), the impact of an alternative indene derivative, ICBA[6], is calculated since it has produced a higher efficiency (6.5% vs. 5.1%) recently as a replacement for C_{60}PCBM with P3HT.[17]

Another factor in the recent increase in device efficiency can be attributed to the development of suitable polymers with bandgaps that extend from the visible into the near-infrared. The embodied energy of polyhexylthiophene (P3HT)[8] is compared to two types of "low bandgap" block copolymers: a polybenzodiathiazole (PTCDTBT)[9] and a poly(benzo[1,2-b:4,5-b']dithiophene)s (PTB7)[10]. These two block copolymers are selected based upon the demonstrated device efficiencies of 6.1 % and 7.4% for PTCDTBT and PTB7, respectively.

Two classes of small molecules are compared in this work, namely phtahlocyanines and squaraines. Phthalocyanines (Pc) can be synthesized by reacting the desired metal chloride with either phthalonitrile (to produce ZnPc, InClPc, CuPc, PdPc, SubPc) or phthalic anhydride (to produce AlPcCl). The original Pc synthesis methods required long high temperature reaction (i.e. > 180 °C for 4 hours), and considerable solvents and catalysts. The newer methods developed

largely for electronic applications employ high energy microwave reactors which allow solvent-free reaction, while producing a higher yield of Pc in a shorter amount of time and lowering the amount of required purification steps.[11] Although Pc has shown tremendous potential, it is typically processed using high vacuum equipment; therefore, a second type of small molecule relevant for OPV is one which can be solution-processed for device fabrication. The most successful to date based upon device efficiency is the squaraine derivative 2,4-bis[4- (N,N-diisobutylamino)-2,6-dihydroxyphenyl]squaraine (SQ).[12] This structure is produced through condensation of an aniline intermediate with squaric acid.

Various interfacial materials are used to improve the electrode contacts in order to enhance charge collection of electrons and holes in organic photovoltaics. For organic photovoltaics, the material inventory for solution processed TiO_x (HBL)[13] is calculated in the present study, while previous published values are used for PEDOT:PSS (EBL)[14] and ZnO (EBL).[15] In the case of small molecules, the CED of bathophenanthroline (BPhen), bathocuproine (BCP), and MoO_3 are each calculated.

Fullerenes

The most common acceptor molecules for organic photovoltaics are fullerenes, either in their native form for small molecule photovoltaics or structurally modified (e.g. PCBM, ICBA, etc.) for polymer photovoltaics. In the recent analysis, the fullerene embodied energy from four production methods was detailed,[5] and has been summarized in ***Figure 43***. There are several prevalent methods to synthesize fullerenes, including plasma techniques (arc and RF), as well as pyrolysis of carbon precursors [(toluene and 1,2,3,4-tetrahydronaphthalene (tetralin)]. The main production method for fullerenes is pyrolysis,[16] so the base case scenario assumes 90% of the fullerene mix from pyrolysis with an equal weighting between carbon precursors. The best case scenario assumes that all fullerenes are produced from pyro-tetralin, which was the method previously reported to have the lowest embodied energy for production[5]. In comparison, the worst-case scenario increases the proportion of fullerenes produced from the two plasma methods from 10 in the base scenario to 20% of the total mix.

As illustrated, C_{70} structures (both native and functionalized) have consistently higher embodied energy than C_{60} ones. There are also significant differences between the modified and native fullerenes, where the "Best" case PCBM scenario for each structure is higher than the worst case native one (e.g. C_{60}PCBM is more than double the embodied energy for pure C_{60}). The comparison between PCBM and ICBA derivatives shows that the ICBA derivatives have a dramatically lower embodied energy, on the order of 40% less for both C_{60} and C_{70} structures. Such a reduction is attributed to a simpler reaction scheme for ICBA derivatives based upon fewer chemicals required during synthesis and processing which results in less embodied energy to produce.

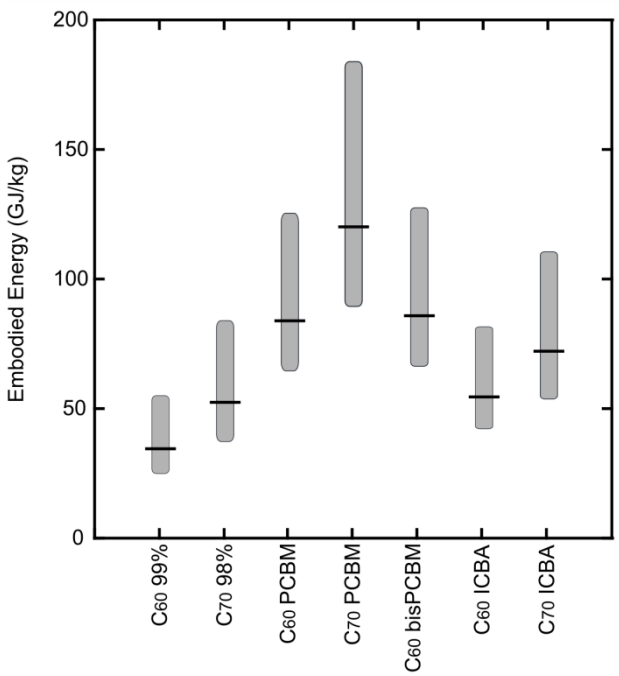

Figure 43: Embodied energy of fullerenes and fullerene derivatives used in organic photovoltaics where the grey bar indicates the best and worst case scenarios and the line, the base case.

The semiconducting polymers used in OPV require multiple steps to build the specific monomer prior to the final polymerization stage. This is illustrated in ***Figure 44*** for three types of semiconducting polymers commonly used to achieve the highest efficiencies to date. Increasing the number of steps from 5 for P3HT to 12 for PTB7 increases the embodied energy by 2.5. In comparison, many common polymers in the chemical industry have 1-2 steps, resulting in an embodied energy typically less than 20 MJ/mol. However, it is important to recognize that even with the additional energy required for multiple synthesis steps, the total embodied energy of each of the commonly used semiconducting polymers for OPV is significantly less than for fullerenes, ranging from 1959 MJ/kg for P3HT to 5848 MJ/kg for PCDTBT. It is evident at this stage of the analysis, that when similar amounts of polymer and fullerene are used in an organic photovoltaic (which is often the case), the fullerene embodied energy will dominate the active layer impact. Thus, in this case, the polymer embodied energy is less than 2.5% of the active layer and it is reasonable to estimate the energy for the other block copolymers with similar number of synthesis steps.

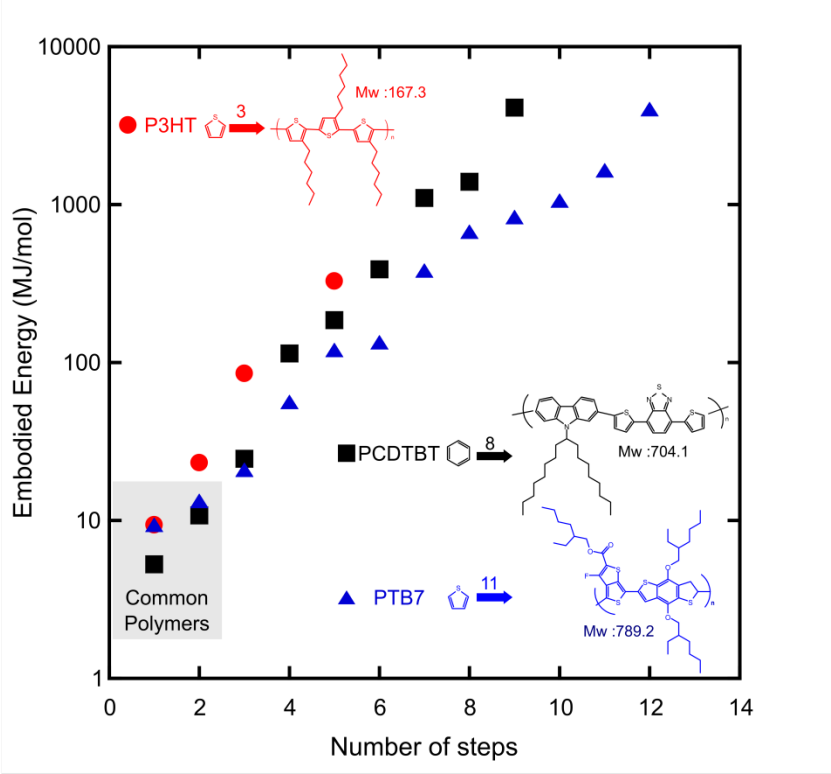

Figure 44: Embodied energy of 3 types of semi-conducting polymer used in organic photovoltaics as a function of synthesis stage.

Small molecules

Each of the phthalocyanine small molecules have 2 synthesis steps and there is a small contribution in each case to the type of coordinated metal atom present. The embodied energy is nearly the same between the small molecules examined, except for PdPc due to the scarcity of palladium (see ***Figure 44***). The comparison between SQ and Pc small molecules shows very similar embodied energy values, thus indicating that any difference in cumulative energy demand from the photovoltaic device will largely depend on the type and extent of processing methods employed.

Interface materials

There are several prevalent interfacial materials being used to improve charge collection in organic photovoltaics either in a single junction device or as a junction between the two devices in a tandem photovoltaic. ***Figure 45*** summarizes the embodied energy of each interface material used in this work. In the case of solution processed interface materials for polymer photovoltaics like TiO_x, ZnO, and PEDOT:PSS, the major component is the solvent since dilute solutions (15-30 mg/mL) are necessary to achieve a layer less than 20 nm during deposition. TiO_x has a higher embodied energy than the other two materials since it uses a sol-gel process during synthesis with a solution that must be refluxed with a ligand.[13] Comparison of BCP and BPhen shows

similar embodied energy since they have similar structure and require the same number of synthesis steps. Overall, the interfacial layers have the lowest impact of typical active materials in the device, and since they are used in small quantities, they are unlikely to have a dominant contribution.

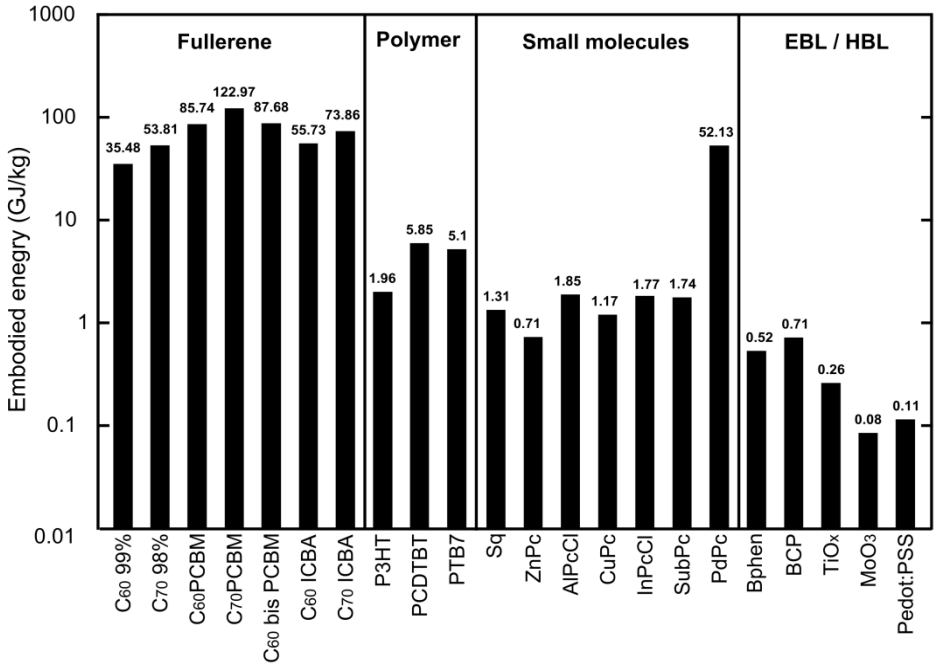

Figure 45: Embodied energy for all types of material considered in this work.

The CED for photovoltaics will be calculated using the embodied energy of the individual materials according to the particular processing conditions.

Hyperspectral Polymer Photocells

There are several challenges restricting the commercial viability of state-of-the-art polymer solar cells involving derivatized fullerene-polymer blends, most notably the device efficiencies and environmental stability of active materials. There is considerable work currently underway to address both of these issues with recent improvement in the latter challenge through the use of improved sealants and passivating barriers. The overall efficiencies of these types of devices, although experiencing steady improvement, are still modest in comparison to other cell technologies. Semi-empirical modeling indicates that the maximum theoretical efficiencies of typical derivitized fullerene/conjugated polymer solar cells will be quite limited due to the poor match to the solar spectrum. The maximum efficiency for PCBM[70]-MEH-PPV and PCBM[60]-P3HT systems, for example, is calculated to be between 6 and 8% under 1 sun AM1.5 illumination. However, the incorporation of NIR absorbing molecules in the range of 800-900 nm can theoretically increase the power conversion efficiency of a single distributed heterojunction polymer solar cell up to 16% under a 1 sun AM1.5 illumination. The objective of

this research is to produce a series of single junction polymeric solar cells using different NIR absorbing molecules and combine them using nanocrystalline tunnel junctions to produce the polymeric analog to a multi-junction III-V solar cell.

Analysis of Candidate NIR Absorbing Dyes by Cyclic Voltammetry

Several dyes (including phthalocyanines, porphyrins, cyanines) were tested for absorbance, HOMO-LUMO level compatibility, and in go/no-go tests in single junction devices. None were as effective as the squaraines. The following dyes were successfully synthesized and purified in house, and characterized in solution.

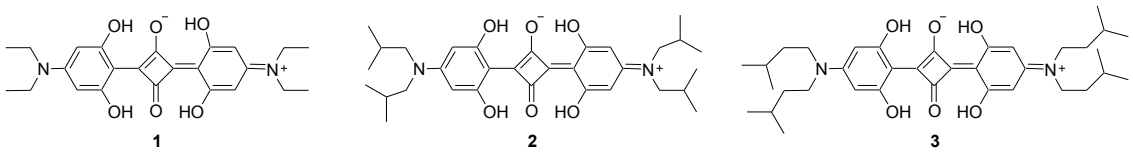

Figure 46: Squaraines 2,4-Bis-(4-diethylamino-2,6-dihydroxy-phenyl)-cyclobutane-1,3-dione, $DESQ(OH)_2$ (1) 2,4-Bis-(4-diisobutylamino-2,6-dihydroxy-phenyl)-cyclobutane-1,3-dione, $DiBSQ(OH)_2$ (2) and 2,4-Bis-(4-diisopentylamino-2,6-dihydroxy-phenyl)-cyclobutane-1,3-dione, $DiPSQ(OH)_2$ (3).

Measurement the Cyclic Voltammograms under Dark/Illuminated Conditions

Once the decision was made to concentrate fully on squaraine dyes, measurement of cyclic voltammograms of their films is precluded because the squaraines are soluble in too wide a variety of solvents. Nevertheless squaraine dyes in solution have been measured using cyclic voltammetry, with results given in *Table **6***.

Table 6: Energy levels of importance measured in eV. a – HOMO measured from cyclic voltammetry in acetonitrile solution, b – LUMO measured from cyclic voltammetry in acetonitrile solution, c – Absorbance onset for solution in chloroform, d – absorbance onset from film, e – bandgap measured from cyclic voltammetry in acetonitrile solution, f – estimated HOMO, g – estimated LUMO.

Dye	HOMO [a](sol)	LUMO[b] (sol)	Opt.[c] Eg(sol)	Opt.[d] Eg(film)	EChem Bandgap[e]	HOMO [f](f, est.)	LUMO [g](f, est.)
Dissobutyl (**2**)	5.66	4.26	1.79	1.4	1.40	5.99	4.59
Diisopentyl(**3**)	5.65	4.18	1.80	1.4	1.47	5.94	4.55
Diethyl (**1**)	5.75	4.25	1.80	1.4	1.51	6.03	4.63

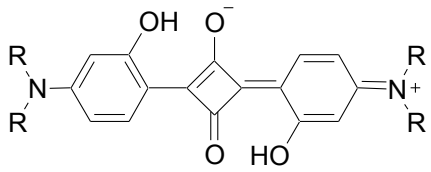

Figure 47: Squaraines 2,4-Bis-(4-dibutylamino-2-hydroxy-phenyl)-cyclobutane-1,3-dione, "SQ44OH" where R=4, and 2,4-Bis-(4-dipentylamino-2-hydroxy-phenyl)-cyclobutane-1,3-dione, "SQ55OH" where R=5.

These molecules were then incorporated into single junction bulk heterojunction solar cells with PCBM and then into tandem devices with a P3HT:PCBM active layer. *Figure **48*** and *Table **7*** show results of successful device manufacture using a comparable squaraine dye, SQ55OH.[1]

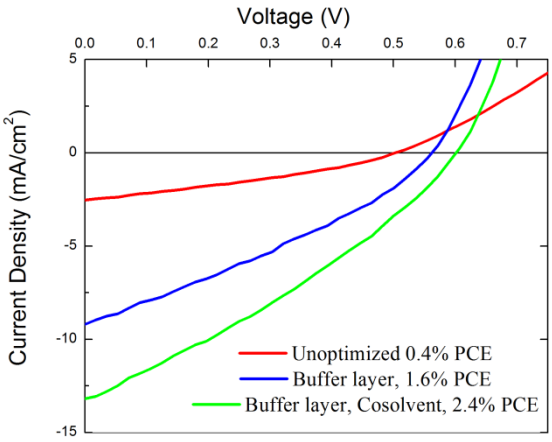

Figure 48: a) I-V curves for a series of SQ55OH:PCBM (3:7 wt. % ratio) devices. The IV characteristics and PCEs are shown in Table 1 below. The unoptimized device (red) was prepared with no cathode buffer layer [PCE=0.4%]. Incorporation of a cathode buffer layer (blue) of optimized thickness 10 nm allows increase in short circuit current [PCE=1.6%]. The best device (black solid line) was fabricated with the cathode buffer layer (d=10 nm) and tetrohydrofuran as co-solvent [PCE=2.4%].

[1] provided by Dr. Kevin Belfield at the University of Central Florida

Device name	J_{sc} (mA/cm^2)	V_{oc} (V)	Fill Factor	Efficiency
Unoptimized SQ:PCBM	2.53	0.503	32.8%	**0.4+/- 0.2%**
SQ:PCBM:Alq3	8.95	0.562	32.1%	**1.6+/- 0.3%**
SQ:PCBM:THF cosolvent:Alq3	13.18	0.601	31.3%	**2.4+/- 0.3%**

Table 7: Current-voltage data, fill-factor and PCEs for SQ55OH:PCBM (3:7 wt. % ratio) bulk heterojunction devices made by the Collison group.

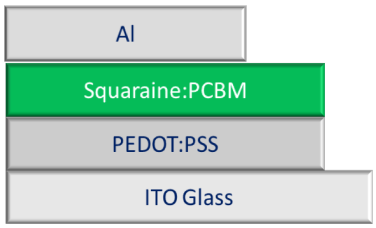

These results show the improvement of device efficiency because of notable process improvements facilitated through use of co-solvents and Alq3 buffer layers, which took into account the ability to control aggregation through morphology change as evidenced, largely, by optical absorption data.

The same gains in efficiency can be achieved through thermal annealing (compared with co-solvent use) and while Alq3 usage is always an option for fully optimized publication ready test cells we typically remove Alq3 so as to streamline the process and reduce total evaporator time, and evaporator maintenance.

Measurement of the spectral response for devices prepared from dye-polymer composites

Annealing of squaraine dyes led to aggregation of the molecules. Aggregation has been shown to improve current density in current voltage curves, and changes in spectral response have been correlated with changes in device efficiency as a result of this aggregation. (Spencer et al in Progress in Photovoltaics 2012) for SQ55OH. More recent data, described below, illustrates how spectral response data can be used to investigate more accurate theories for device limitations associated with charge transfer kinetics that are a function of aggregate type.

For the purpose of investigating the impact of aggregates formation or morphology of the Squaraine/PCBM active layer on the efficiency of photovoltaic devices, 3 sets of samples were measured for spectral response to get the external quantum efficiency on the whole spectrum. Each set contained at least four repeated samples, so the quantum efficiency value of aggregate peaks could be obtained. The samples were set up as DPSQ/PCBM (diisopentyl, dihydroxy squaraine blended with PCBM), unannealed, annealed at 165° for 60 seconds and annealed at 180° for 60 seconds. The curves in ***Figure 49*** for these three sets of samples were obtained using the representative data of all the repeated samples.

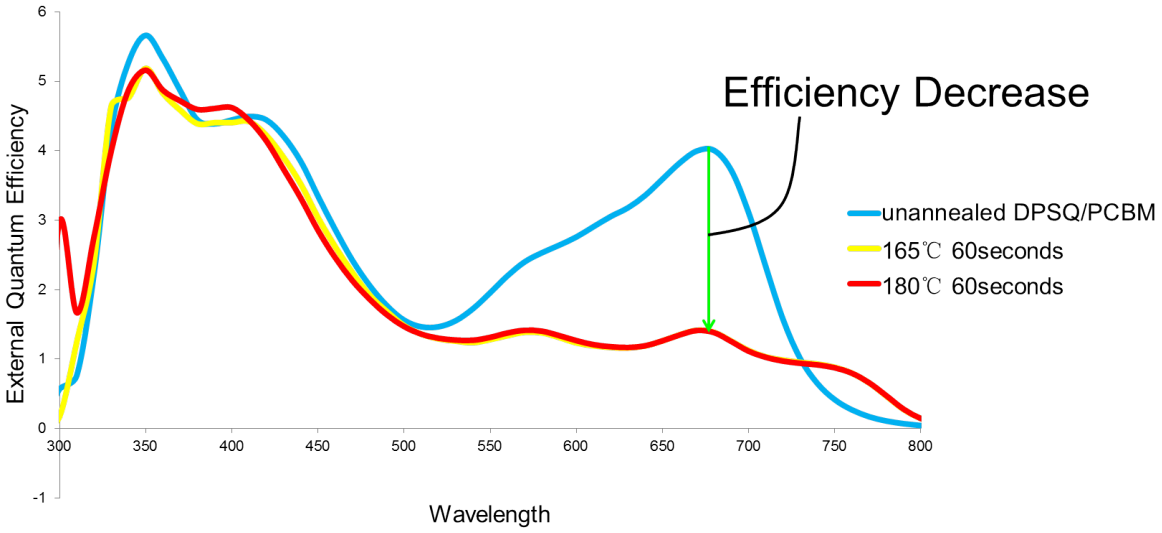

Figure 49

From *Figure **49*** a huge loss of quantum efficiency upon thermal annealing can be observed on the spectrum in the range of 500nm to 720nm, in the spectrum range above 720nm, the quantum efficiency is slightly increased after thermal annealing treatment, but the overall quantum efficiency of the DPSQ Squaraine ($DiPSQ(OH)_2$) is substantially decreased because of thermal annealing. Work describing the theoretical implications and the overlap with Marcus-Hush theory for reduced rates of charge photogeneration has been developed and has been submitted for publication to the Journal of Physical Chemistry C (American Chemical Society). These results are the basis for further expanded investigation using squaraines and their aggregation to probe for a better understanding of the mechanisms behind small molecule organic photovoltaics. These results are the basis for further expanded theoretical investigation in collaboration with Frank Spano at Temple University (Proposal titled, " DMREF - Collaborative Research: Prescriptive Design of Squaraine Derivatives Optimized for Photoinduced Charge Transfer and 2-Photon Absorption", submitted to NSF February, 2014).

Optimization of Active Layer Composition to Maximize Absorption and Charge Transport

Charge transport studies using field effect transistors and Time of Flight Transient Photoconductivity were carried out for P3HT and PCBM blends. It was hypothesized that the mobility of active layer materials was a major contributor towards improved device performance. Since most organic photovoltaic materials have relative low mobility, falling into the 10^{-3} to 10^{-6} $cm^2/(V•s)$ range, standard methods of mobility measurement for silicon-based devices are no longer suitable for organic materials. Therefore we built an instrument that measures the mobility of organic active layers, using Time of Flight Transient Photoconductivity (TOF). By measuring the travel time of a charge carrier layer generated by a short laser pulse in a sample of known thickness, the mobility of P3HT can be successfully extracted.

The electric-field dependence of the charge carrier mobility was thus studied, and was hypothesized to match the Poole–Frenkel model. In experiments that were conducted, a certain percentage of PCBM was doped into P3HT and a correlation between PCBM concentration and mobility in the mixture of materials was sought. The same blend ratios of PCBM:P3HT would be used for making actual photovoltaic devices, whose power conversion efficiency (PCE) and external quantum efficiency (EQE) would be demonstrated. This work would thus investigate the connection between mobility, PCE, EQE and blend ratio, which, it was hoped, would significantly provide a better understanding of device performance and show a clearer path to improve organic photovoltaic efficiency.

Our ultimate goal for TOF Transient Photoconductivity was to find the point at which electron mobility in PCBM is matched by hole mobility in P3HT.

Since P3HT is considered the primary hole conductor and PCBM the primary electron conductor in a bulk heterojunction device, it was expected that a balance point would exist as PCBM:P3HT blend ratio changed, whereby the hole mobility and electron mobility would be equivalent. The hope was to compare the results of mobility measurements with photovoltaic efficiency. Hence, one could clarify whether this mobility balance would benefit device efficiency. In addition, according to the Poole-Frenkel model, electric-field dependence of the charge carrier mobility diminishes as $\mu=\beta E^{1/2}$, where μ is mobility and E is the electric field strength. β should be negative at room temperatures. This would also be studied.

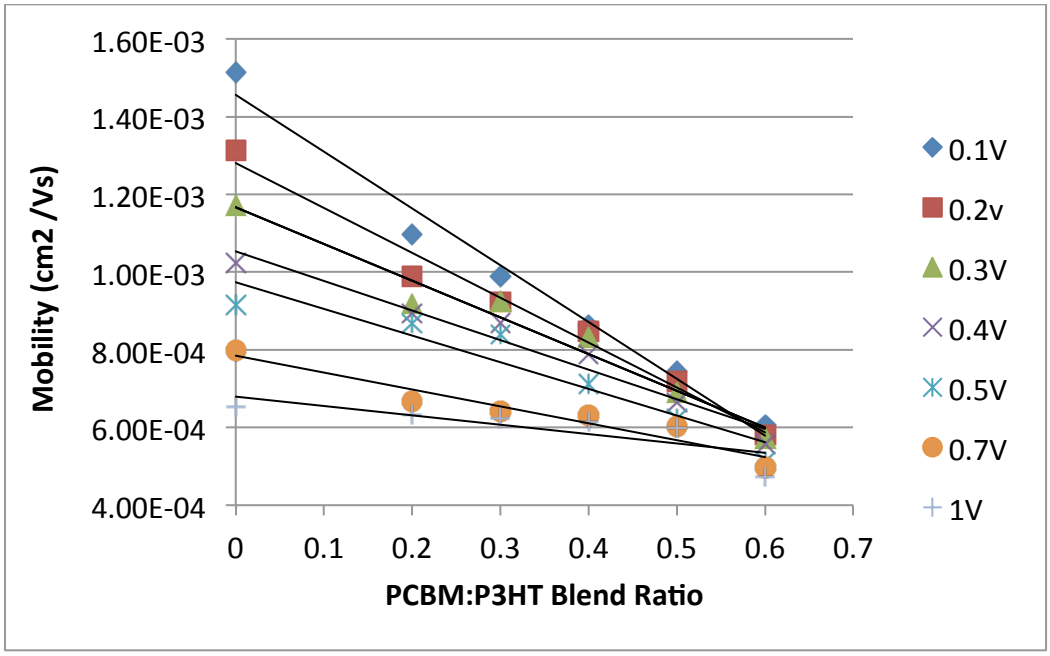

Figure 50: Mobility measurements made using Time of Flight transient photoconductivity measurements of blended PCBM and P3HT.

Time of Flight Transient Photoconductivity measurements gave rise to the mobilities shown in *Figure **50***. As shown, by increasing the PCBM proportion in PCBM:P3HT films, the hole mobility decreased, as expected. This is explained in that the PCBM molecule would create a recombination source for hole charge carriers and the potential barrier at the PCBM:P3HT interface may slow down the ability of the charges to move through the device. Also consistent with the data, by doping more PCBM into the film, the morphology of the P3HT will change; a broken polymer chain or a gap between chains may occur. Such morphology changes will diminish hole mobility either along the chains or from jumping between chains.

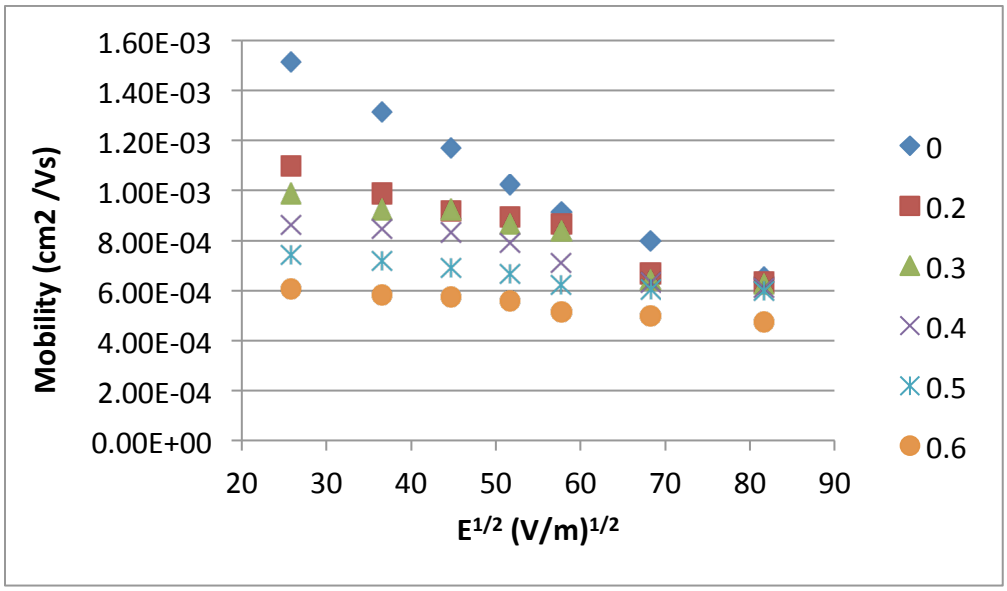

Figure 51: Mobility of PCBM:P3HT blend samples of varying weight percent of PCBM plotted as a function of the square root of the applied electric field. Different symbols indicate the blend ratio of the films under investigation.

Measured mobilities are also shown in *Figure **51*** in a way that allowed for the appropriate charge transport model to be investigated. *Figure **52*** also shows mobilities at 0.5 V applied field, and power conversion efficiencies for analogous devices plotted as a function of blend ratio. Based on these data, hole mobility decreases with increasing PCBM content. Subsequently, the larger the applied electrical field, the smaller the mobility, which matches the assumptions in low field associated with the "Poole Frenkel" theory. β is positive at temperatures around 250–270 K, and β becomes negative at higher temperatures. The data clearly show the slope as negative for increasing fields. Beside the effect of temperature, the magnitude of electric field would also affect the β value. However this effect will only occur when $E^{1/2}$ is larger than 700, and so will likely not be significant in the case of an OPV device.

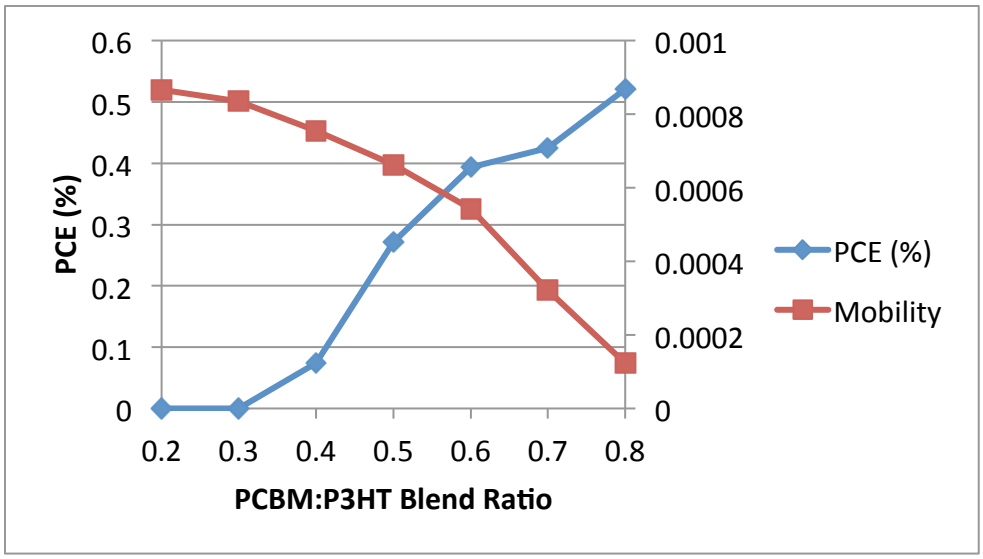

Figure 52: A plot of mobility at 0.5V applied voltage versus power conversion efficiency for analogous devices.

As shown in the figure above, the higher the percentage of PCBM doped in the active layer, the higher the efficiency. Unfortunately, in these experiments, the solubility of PCBM limits the possibility of measuring mobility for larger blend ratios. There is clearly more to measure and to discuss but the data remains consistent with the general idea that balancing mobility of electrons and holes reduces the carrier recombination rates.

In summary, data was interpreted in that a hopping model would be better utilized than a "band theory with traps model." The model used is critical since the mobility governs the charge transport in organic photovoltaics.

In general, many efforts were typically associated with improving and eventually optimizing working devices by varying solution concentrations, film thicknesses and blend ratios. Work to measure charge transport properties of *squaraine* films using Time of Flight Transient (TOF) photoconductivity measurements was hampered by the fundamental inability to get thick enough films for accurate mobility measurements. Eventual success was achieved through collaboration with G. Rumbles and O. Reed at NREL in measurements of Time Resolved Microwave Conductivity, with those results submitted for publication. Results linking the reduction in external quantum efficiency in the red part of the solar spectrum have been presented at the 245th ACS National Meeting and Exposition, April 7-11, 2013, New Orleans, Louisiana and will be published.

Understanding of how Processing Conditions Affects the Active Film Properties

As part of a more robust investigation of film morphology in films of different thicknesses and, in particular, after study of our standard 100nm films using TEM through collaborations, we noticed unusual patterns of phase separation as a result of our annealing process. We therefore

plan to investigate this more thoroughly using TEM and powder X-Ray Diffraction measurements.

Ongoing work with squaraine devices has led to a substantial correlation between extent of crystallinity, aggregation and excited state properties, and the efficiency of the NIR-absorbing devices. The work demonstrates that exciton dissociation at the bulk heterojunction is a critical rate-limiting step in small molecule devices, and that squaraines are highly selective energetic and spatial probes of this crucial charge-generating process. Focus has thus been placed exclusively upon squaraine films and devices as opposed to polymer morphological studies, which are being studied far more competitively by multiple groups in the field.

Development of Tandem Junction Polymer Solar Cells

TiOx has been successfully employed with similar tandem devices. A synthesis of TiOx sols was procedurally tightened to increase the shelf-lives and predictability of gel-films made from these sols. Work to improve our processing of TiO_x in Tandem P3HT:PCBM-only devices was halted, with more emphasis having been placed on improving the reproducibility of processing for single junction devices. Indeed, major gains were made through the expansion of work with squaraine based solution processable bulk heterojunction devices as a result of a sensible focus on developing a more robust process for manufacturing single junction devices. This was necessary simply because there were too many variables associated with manufacture of tandem devices; there were too many parameters, each of which would contribute to the efficiency of a device and without optimal process control and mechanistic understanding of our small molecule devices we would not be able to make solid ground in identifying limiting factors for tandem device efficiencies.

Investigation of SWCNT Replacement of ITO in MEH-PPV:PCBM and P3HT:PCBM Devices

Efforts pertaining to the use of single walled carbon nanotube (SWCNT) films as a potential replacement for ITO focused on improving control and reproducibility in film preparation and successful application to flexible substrates. We continue to investigate how thermal oxidation parameters and dispersion procedures commonly employed in the purification and isolation of carbon nanotubes have enormous impact on film performance. Samples of nanotubes are typically subjected to sonication in dimethylacetamide (DMA) following thermal oxidation. Following sonication, the resulting suspensions are filtered, washed, and dried, then employed to prepare new dispersions of the SWCNTs in 2-propanol, employing 2-hydroxypropyl cellulose as a polymeric surfactant. These dispersions were used to prepare films by spray coating.

Reproducibility has been very poor, with several additional parameters beyond the heterogeneity of the nanotube sample (spray-coater settings, distance of coater from films, choice of sonicator) having a major impact to spread in sheet resistance and transmission. As a result, large sample sizes are needed in order to provide a statistically meaningful result. Results have been inconclusive and the need for such large numbers of measurements to confirm theories and hypotheses have stifled progress in this area.

Publications & Presentations

Adams, Jessica G. J., Victor C. Elarde, Glen Hillier, Christopher Stender, Francis Tuminello, Andree Wibowo, Chris Youtsey, et al. 2013. "Improved Radiation Resistance of Epitaxial Lift-Off Inverted Metamorphic Solar Cells." In *2013 IEEE 39th Photovoltaic Specialists Conference (PVSC)*, 3229–3232. IEEE. doi:10.1109/PVSC.2013.6745140.

Bailey, CG, DV Forbes, and SJ Polly. 2011. "Optical and Mechanical Properties of Strain Compensated InAs/GaAs Quantum Dot Superlattices with Varying InAs Coverage." *Submitted: Journal of Cystal Growth*.

Bailey, Christopher G., David V. Forbes, Matthew P. Lumb, Michael K. Yakes, Maria Gonzalez, Joseph G. Hubbard, Seth M. Hoheisel, Raymond Tischler, Igor Vurgaftman, Jerry R. Meyer, and Robert J. Walters. 2013. "Incorporation of InGaAs Quantum Wells in an InP Lattice-Matched 1 eV InAlGaAs n-i-p Solar Cell." In *39th IEEE Photovoltaic Specialists Conference*, 16–21.

Bailey, Christopher G., David V. Forbes, Ryne P. Raffaelle, and Seth M. Hubbard. 2011. "Near 1 V Open Circuit Voltage InAs/GaAs Quantum Dot Solar Cells." *Applied Physics Letters* 98 (16): 163105. doi:10.1063/1.3580765.

Bennett, Mitchell F., Zachary S. Bittner, David V. Forbes, Rao Tatavarti, Andree Wibowo, Noren Pan, Kevin Chern, and Seth M. Hubbard. 2013. "Alpha Radiation Effects on n-i-p Quantum Dot Epitaxial Lift-Off Solar Cells." In *2013 IEEE 39th Photovoltaic Specialists Conference (PVSC)*, 2784–2789. IEEE. doi:10.1109/PVSC.2013.6745050.

Collison, C. 2013. "Squaraines for Mechanistic Studies and Improved Efficiency of Bulk Heterojunction Organic Photovoltaic Devices." *SUNY Brockport*, February 14.

Collison, C., S.D. Spencer, V. Murcia, B. Zhu, P. Heaphy, and J. Cody. "Systematic Squaraine Modification and Morphology Control for Competitive Solution-Processable Bulk Heterojunction Devices in the Near Infra-Red." In *MRS National Fall Meeting, Boston, MA, United States, November 26-November 30, 2012, Symposium H: Small-Molecule Organic Solar Cells. H8.23*.

Collison, C.J., J. Cody, S.D. Spencer, A. Ioannidis, A. Monfette, H. Hu, and B. Zhu. 2011. "The Impact of Squaraine Functionalization on the Efficiencies of NIR-Active Bulk Heterojunction Photovoltaics." In *SPIE 2011 Optics and Photonics, Photonic Devices and Applications, Organic Photovoltaics XII*, 8116–95.

Collison, CJ, SD Spencer, A Monfette, J Alexander, and J Staub. 2010. "New Candidates for Near-Infra-Red-Absorbing Active Layers in Multijunction Organic Photovoltaics: Characterization and Performance." In *2010 35th IEEE Photovoltaic Specialists Conference*, 001601–001606. IEEE. doi:10.1109/PVSC.2010.5616388.

DiLeo, Roberta A., Sarah Frisco, Matthew J. Ganter, Reginald E. Rogers, Ryne P. Raffaelle, and Brian J. Landi. 2011. "Hybrid Germanium Nanoparticle–Single-Wall Carbon Nanotube Free-Standing Anodes for Lithium Ion Batteries." *The Journal of Physical Chemistry C* 115 (45) (November 17): 22609–22614. doi:10.1021/jp205992w.

Forbes, David V., Christopher G. Bailey, Stephen Polly, Zachary S. Bittner, Chris Kerestes, Michael Slocum, and Seth M. Hubbard. 2012. "Correlation Between Quantum Dot Morphology and Photovoltaic Performance." In

2012 38th IEEE Photovoltaic Specialists Conference, 001798–001802. IEEE. doi:10.1109/PVSC.2012.6317942.

Forbes, David V., Christopher Bailey, Stephen J. Polly, Adam Podell, and Seth M. Hubbard. 2013. "The Effect of GaAs Capping Layer Thickness on Quantum Dot Solar Cell Performance." In *2013 IEEE 39th Photovoltaic Specialists Conference (PVSC)*, 3203–3207. IEEE. doi:10.1109/PVSC.2013.6745134.

Ganter, M., G. Gaustad, C. Babbitt, and B. Landi. 2013. "Recovery and Refunctionalization of LiFePO4 Cathode from End-of-Life Commercial Lithium Ion Batteries." In *Battery Recycling Symposium, The Minerals, Metals, and Materials (TMS) Annual Conference*. San Antonio, TX.

Huang, Y, TW Kim, S Xiong, and LJ Mawst. 2013. "InAs Nanowires Grown by Metal–Organic Vapor-Phase Epitaxy (MOVPE) Employing PS/PMMA Diblock Copolymer Nanopatterning." *Nano Letters* 13 (12): 5979–5984.

Hubbard, Seth M., Mitchell Bennett, Adam Podell, and David V. Forbes. 2012. "Optimization of Growth and Device Performance for InAs Quantum Dot Solar Cells." In *2012 38th IEEE Photovoltaic Specialists Conference*, 001788–001793. IEEE. doi:10.1109/PVSC.2012.6317940.

Hubbard, SM, A Podell, and C Mackos. 2013. "Effect of Vicinal Substrates on the Growth and Device Performance of Quantum Dot Solar Cells." *Solar En* 108: 256–262.

Kerestes, Christopher, Stephen Polly, David Forbes, Christopher Bailey, Seth Hubbard, John Spann, Pravin Patel, and Paul Sharps. 2011. "Investigation of Quantum Dot Enhanced Triple Junction Solar Cells." In *2011 37th IEEE Photovoltaic Specialists Conference*, 000127–000132. IEEE. doi:10.1109/PVSC.2011.6185860.

Laghumavarapu, Ramesh B., Baolai L. Liang, Zachery Bittner, Tugba S. Navruz, Seth M. Hubbard, Andrew Norman, and Diana L. Huffaker. 2013. "GaSb/InGaAs Quantum Dot-Well Solar Cells." In *2013 IEEE 39th Photovoltaic Specialists Conference (PVSC)*, 0292–0295. IEEE. doi:10.1109/PVSC.2013.6744150.

Landi, B. 2011a. "Carbon Nanotubes for Lithium Ion Batteries and Cables." In *Carbon Nanotubes for Space Applications Interchange Meeting 2011*. Washington, D.C.

Mackos, CR, and DV Forbes. 2011. "GaAs Substrate Misorientation and the Effect on InAs Quantum Dot Critical Thickness." In *Photovoltaic Specialists Conference (PVSC), 2011 37th IEEE*, 1–6.

Murcia, V. M., S. D. Spencer, B. Zhu, P. Heaphy, J. A. Cody, and C. J. Collison. 2012. "Characterization of H- and J- Aggregates and Their Impact on Squaraine-Based Bulk Heterojunction Organic Photovoltaics." In *NERM ACS*.

Murcia, VM, SD Spencer, M Hall, JA Cody, and CJ Collison. "Effect of Alkyl Side-Chain Length on Aggregate Formation and PCBM Interaction for a Series of Squaraine Dyes Targeted for Organic Photovoltaic Applications." In *MRS National Fall Meeting, Boston, MA, United States, December 1-6, 2013 Y9.27 Physics of Organic and Hybrid Organic-Inorganic Solar Cells*.

Polly, S.J., D.V. Forbes, K.M. Driscoll, and S.M. Hubbard. 2013. "Delta Doping Effects on Quantum Dot Solar Cells." In *IEEE 39th Photovoltaic Specialists Conference (PVSC)*, 16–21.

Polly, Stephen J., Zachary S. Bittner, Mitch F. Bennett, Ryne P. Raffaelle, and Seth M. Hubbard. 2011. "Development of a Multi-Source Solar Simulator for Spatial Uniformity and Close Spectral Matching to AM0

and AM1.5." In *2011 37th IEEE Photovoltaic Specialists Conference*, 001739–001743. IEEE. doi:10.1109/PVSC.2011.6186290.

Richards, B. C., Yong Lin, Pravin Patel, Daniel Chumney, Paul R. Sharps, Chris Kerestes, David Forbes, Kristina Driscoll, Adam Podell, and Seth Hubbard. 2013. "Performance and Radiation Resistance of Quantum Dot Multi-Junction Solar Cells." In *IEEE 39th Photovoltaic Specialists Conference (PVSC)*, 0158–0161. IEEE. doi:10.1109/PVSC.2013.6744119.

Slocum, Michael A., David V. Forbes, Mihir H. Bohra, and Seth M. Hubbard. 2013. "An Evaluation of Fabrication Methods for Doping Superlattice Devices." In *2013 IEEE 39th Photovoltaic Specialists Conference (PVSC)*, 1727–1732. IEEE. doi:10.1109/PVSC.2013.6744477.

Spencer, S., C. Bougher, BR. Conrad, J. Cody, J. Andersen, S. Misture, and C. Collison. "Experimental Study on the Applicability of Marcus-Hush Theory for Squaraine Aggregate Donors to Explain the Photophysics of Exciton Dissociation at the Bulk Heterojunction Interface." In *MRS National Fall Meeting, Boston, MA, United States, December 1-6, 2013, Y3.13/N3.13 Functional Aspects of Luminescent and Photoactive Organic and Soft Materials/ Physics of Organic and Hybrid Organic-Inorganic Solar Cells*.

Spencer, S. D., V. M. Murcia, J. A. Cody, B. R. Conrad, J. Andersen, P. J. Heaphy, and C. J. Bougher. 2012. "Squaraine Dye Aggregation: Impact of Thermal Annealing on Nanomorphology and Organic Solar Cell Device Performance." In *286 ACS 38th NERM*. Rochester, NY USA.

Spencer, Susan D., Cortney Bougher, Patrick J. Heaphy, Victor M. Murcia, Cameron P. Gallivan, Amber Monfette, John D. Andersen, Jeremy A. Cody, Brad R. Conrad, and Christopher J. Collison. 2013. "The Effect of Controllable Thin Film Crystal Growth on the Aggregation of a Novel High Panchromaticity Squaraine Viable for Organic Solar Cells." *Solar Energy Materials and Solar Cells* 112 (May): 202–208. doi:10.1016/j.solmat.2013.01.008.

Spencer, Susan, Victor Murcia, Obadiah Reid, Garry Rumbles, Kevin Belfield, Jeremy Cody, and Christopher Collison. 2012. "Influence of Squaraine Aggregation on Short-Circuit Current and Device Efficiency." In *2012 38th IEEE Photovoltaic Specialists Conference*, 002775–002779. IEEE. doi:10.1109/PVSC.2012.6318168.

Spencer, Susan, Jason Staub, Amber Monfette, and Christopher Collison. 2011. "Characterization and Performance of a Novel Squaraine Dye Near-Infrared Absorbing Layer in a Tandem Bulk Heterojunction Photovoltaic Device." In *MRS National Spring Meeting*. San Francisco, CA, United States.

Spencer, Susan, Chenyu Zheng, Patrick Heaphy, Cortney Bougher, Julian Williams, Brad Conrad, Scott Misture, John Andersen, Jeremy Cody, and Chris Collison. 2013. "Self-Assembling Squaraine Aggregates' Impact on Photovoltaic Performance." In *Organic Optoelectronics, 55th Materials Research Society Electronic Materials Conference (EMC)*. University of Notre Dame, South Bend, Illinois, USA.

Wolfe, GE., C. Zheng, VM. Murcia, SD. Spencer, JA. Cody, and CJ. Collison. "Use of Photophysical Properties of Novel Squaraines to Screen for Their Viability in Organic Solar Cells." In *MRS National Fall Meeting, Boston, MA, United States, December 1-6, 2013, Y3.11/N3.11 Functional Aspects of Luminescent and Photoactive Organic and Soft Materials/ Physics of Organic and Hybrid Organic-Inorganic Solar Cells*.

Zheng, C., G. Wolfe, V. Murcia, SD. Spencer, JA. Cody, and CJ Collison. "Chemical Modification of Squaraines and Their Photophysical Properties Targeted for Mechanistic Study of Organic Photovoltaics." In *MRS National Fall Meeting, Boston, MA, United States, December 1-6, 2013 Y3.16/N3.16 Functional Aspects of Luminescent and Photoactive Organic and Soft Materials/ Physics of Organic and Hybrid Organic-Inorganic Solar Cells*.

(1) Veldman, D.; Meskers, S. C. J.; Janssen, R. A. J. The Energy of Charge-Transfer States in Electron Donor–Acceptor Blends: Insight into the Energy Losses in Organic Solar Cells. *Advanced Functional Materials* **2009**, *19*, 1939-1948.
(2) Salleo, A.; Chen, T. W.; Völkel, A. R.; Wu, Y.; Liu, P.; Ong, B. S.; Street, R. A. Intrinsic hole mobility and trapping in a regioregular poly(thiophene). *Phys. Rev. B* **2004**, *70*, 115311.
(3) Kim, J. Y.; Lee, K.; Coates, N. E.; Moses, D.; Nguyen, T.-Q.; Dante, M.; Heeger, A. J. Efficient Tandem Polymer Solar Cells Fabricated by All-Solution Processing. *Science* **2007**, *317*, 222 -225.
(4) Park, S. H.; Roy, A.; Beaupre, S.; Cho, S.; Coates, N.; Moon, J. S.; Moses, D.; Leclerc, M.; Lee, K.; Heeger, A. J. Bulk heterojunction solar cells with internal quantum efficiency approaching 100%. *Nat Photon* **2009**, *3*, 297-302.
(5) Anctil, A.; Babbitt, C. W.; Raffaelle, R. P.; Landi, B. J. Material and Energy Intensity of Fullerene Production. *Environmental Science & Technology* **2011**, *45*, 2353-2359.
(6) He, Y.; Chen, H.-Y.; Hou, J.; Li, Y. Indene−C60 Bisadduct: A New Acceptor for High-Performance Polymer Solar Cells. *Journal of the American Chemical Society* **2010**, *132*, 1377-1382.
(7) Zhao, G.; He, Y.; Li, Y. 6.5% Efficiency of Polymer Solar Cells Based on poly(3-hexylthiophene) and Indene-C60 Bisadduct by Device Optimization. *Advanced Materials* **2010**, *22*, 4355-4358.
(8) Stefan, M. C.; Javier, A. E.; Osaka, I.; McCullough, R. D. Grignard Metathesis Method (GRIM): Toward a Universal Method for the Synthesis of Conjugated Polymers. *Macromolecules* **2009**, *42*, 30-32.
(9) Blouin, N.; Michaud, A.; Leclerc, M. A Low-Bandgap Poly(2,7-Carbazole) Derivative for Use in High-Performance Solar Cells. *Advanced Materials* **2007**, *19*, 2295-2300.
(10) Liang, Y.; Feng, D.; Wu, Y.; Tsai, S.-T.; Li, G.; Ray, C.; Yu, L. Highly Efficient Solar Cell Polymers Developed via Fine-Tuning of Structural and Electronic Properties. *Journal of the American Chemical Society* **2009**, *131*, 7792-7799.
(11) Villemin, D.; Hammadi, M.; Hachemi, M.; Bar, N. Applications of Microwave in Organic Synthesis: An Improved One-step Synthesis of Metallophthalocyanines and a New Modified Microwave Oven for Dry Reactions. *Molecules* **2001**, *6*, 831-844.
(12) Wei, G.; Lunt, R. R.; Sun, K.; Wang, S.; Thompson, M. E.; Forrest, S. R. Efficient, Ordered Bulk Heterojunction Nanocrystalline Solar Cells by Annealing of Ultrathin Squaraine Thin Films. *Nano Letters* **2010**, *10*, 3555-3559.
(13) Park, S. H.; Roy, A.; Beaupre, S.; Cho, S.; Coates, N.; Moon, J. S.; Moses, D.; Leclerc, M.; Lee, K.; Heeger, A. J. Bulk heterojunction solar cells with internal quantum efficiency approaching 100%. *Nat Photon* **2009**, *3*, 297-302.
(14) Roes, A. L.; Alsema, E. A.; Blok, K.; Patel, M. K. Ex-ante environmental and economic evaluation of polymer photovoltaics. *Progress in Photovoltaics: Research and Applications* **2009**, *17*, 372-393.
(15) Espinosa, N.; García-Valverde, R.; Urbina, A.; Krebs, F. C. A life cycle analysis of polymer solar cell modules prepared using roll-to-roll methods under ambient conditions. *Solar Energy Materials and Solar Cells* **2011**, *95*, 1293-1302.
(16) Takehara, H.; Fujiwara, M.; Arikawa, M.; Diener, M. D.; Alford, J. M. Experimental study of industrial scale fullerene production by combustion synthesis. *Carbon* **2005**, *43*, 311-319.